

Broadband multiwavelength properties of the archetypal blazar 3C 279 during the 2017 Event Horizon Telescope campaign

Downloaded from: https://research.chalmers.se, 2026-11-24 08:27 UTC

Citation for the original published paper (version of record):
Principe, G., Algaba, J., Aviano, E. et al (2026). Broadband multiwavelength properties of the archetypal blazar 3C 279 during the 2017 Event
Horizon Telescope campaign. Astronomy and Astrophysics, 712.
http://dx.doi.org/10.1051/0004-6361/202659551

N.B. When citing this work, cite the original published paper.

research.chalmers.se offers the possibility of retrieving research publications produced at Chalmers University of Technology. It covers all kind of research output: articles, dissertations, conference papers, reports etc. since 2004. research.chalmers.se is administrated and maintained by Chalmers Library

(article starts on next page)

A&A, 712, A224 (2026)
https://doi.org/10.1051/0004-6361/202659551
© The Authors 2026

Astronomy & Astrophysics

Broadband multiwavelength properties of the archetypal blazar 3C 279 during the 2017 Event Horizon Telescope campaign

G. Principe, J. C. Algaba, E. Aviano, W. Y. Cheong, K. Hada, D. Haggard, A. Hahn, S. G. Jorstad, et al.

(Full author list and affiliations details can be found after the references)

Received 21 February 2026 / Accepted 18 June 2026

ABSTRACT

Context. The archetypal blazar 3C 279 has a prominent relativistic jet and strong broadband variability across the electromagnetic spectrum. In April 2017, the Event Horizon Telescope (EHT) observed 3C 279 with an unprecedented angular resolution of about 20 μas, accompanied by one of the most extensive quasi-simultaneous multiwavelength (MWL) campaigns ever conducted, spanning from radio to TeV γ-ray energies.
Aims. Taking advantage of this comprehensive MWL dataset, we investigated the physical processes governing 3C 279, with a particular focus on the formation, collimation, and acceleration of its relativistic jet and on the origin of its high-energy emission, including the underlying particle-acceleration mechanisms.
Methods. We analyzed individual observations and multiband light curves. We also constructed a new quasi-simultaneous spectral energy distribution covering frequencies from the radio band to very high-energy (VHE) γ rays. We further performed a phenomenological modeling using the turbulent extreme multi-zone (TEMZ) model to constrain the fundamental physical properties of the source.
Results. The EHT observations reveal a clear flux increase in the innermost core between April 5 and 11, 2017. Over a broader time span, radio observations at longer wavelengths reveal concurrent enhancements in the core flux and polarization around mid-April, coinciding with the ejection of a superluminal knot moving at $(25 \pm 2)c$. Record UV–optical flares with strong polarization variability occurred in late March, followed by high-energy γ-ray activity that declined before the end of the EHT observing period. During this time, the source remained in a low X-ray state and exhibited no detectable VHE emission.
Conclusions. The results of the TEMZ modeling indicate that the broadband spectrum and variability of 3C 279 might be explained with a jet scenario in which turbulent plasma cells are compressed by a stationary conical shock. Nonetheless, alternative interpretations, such as magnetic reconnection or a moving shock-in-jet event, remain possible. This coordinated MWL campaign advances our understanding of the origin of the jet and γ-ray emission in the blazar 3C 279, and it also provides a comprehensive publicly available dataset that will serve as a valuable reference for future studies.

Key words. galaxies: active – galaxies: jets – gamma rays: galaxies – quasars: individual: 3C 279

1. Introduction

Flat-spectrum radio quasars (FSRQs) form a subclass of blazars and represent the most powerful active galactic nuclei (AGNs). Their relativistic jets are oriented close to the observer's line of sight, resulting in strongly beamed emission. It remains a central challenge in modern astrophysics to understand the mechanisms of jet launching, collimation, evolution, and how particles are accelerated to GeV and TeV energies in such extreme environments (see, e.g., Blandford et al. 2019 for a review).

Blazars produce broadband nonthermal radiation that extends across the entire electromagnetic spectrum, from radio wavelengths to very high-energy (VHE; $E > 100$ GeV) γ rays. Their radio and optical emission is typically highly linearly polarized (a few up to a few dozen percent; see, e.g., Angelakis et al. 2016) and varies strongly on timescales ranging from minutes to years (Ackermann et al. 2016). Moreover, blazars and jetted AGN constitute the most numerous class of extragalactic γ-ray emitters (Abdollahi et al. 2020), presenting high-energy emission across a wide range of evolutionary stages and spatial scales, from compact subparsec regions (Migliori et al. 2016; Principe et al. 2020, 2021) to more extended kiloparsec-scale structures (Ajello et al. 2020). Among them, 3C 279 is a prominent FSRQ and one of the most distant VHE γ-ray sources, located at a redshift of $z = 0.5362$ (Marziani et al. 1996). At the center of its host galaxy resides a supermassive black hole (SMBH) with an estimated mass of $8 \times 10^8\ M_\odot$ (Nilsson et al. 2009).

The source was first targeted in April 2017 during a four-day campaign while also serving as one of the primary calibrators for the Event Horizon Telescope (EHT) observations of M87* and Sgr A* at 230 GHz (EHT Collaboration 2019a, 2022). The EHT ultra-high angular resolution of 20 μas achieved in these observations corresponds to a spatial scale of 0.13 pc (~1700 Schwarzschild radii). In 2017, the EHT observed 3C 279 in four epochs: April 5, 6, 10, and 11 (Kim et al. 2020). On all days, the data revealed a complex multicomponent morphology in the innermost jet region, with the northernmost feature, identified as the VLBI core, elongated roughly perpendicular to the large-scale jet axis seen at longer wavelengths. The overall morphology might correspond to either a broadened resolved jet base or to a spatially bent jet. The source morphology also varied significantly on timescales of days, indicating systematic structural evolution in the inner jet. Two compact components are observed to move non-radially at apparent superluminal speeds of ~15c and ~20c. Together with inferred Doppler factors of 10–20, these motions support a scenario of traveling shocks or instabilities within a bent and possibly rotating jet. The observed apparent speeds are consistent with measurements at longer (centimeter) wavelengths, suggesting that no substantial jet acceleration occurs between the 1.3 mm VLBI core and the outer jet regions.

Open Access article, published by EDP Sciences, under the terms of the Creative Commons Attribution License (https://creativecommons.org/licenses/by/4.0), which permits unrestricted use, distribution, and reproduction in any medium, provided the original work is properly cited.
This article is published in open access under the Subscribe to Open model. Subscribe to A&A to support open access publication.

Several mechanisms have been proposed to explain the jet bending at these scales. In thin-disk systems such as 3C 279, jet precession might arise from Lense–Thirring torques in a misaligned accretion flow (Liska et al. 2018, 2021). Alternatively, jet wobbling can be driven by magnetic eruptions associated with reconnection near the event horizon (e.g., Ripperda et al. 2022; Ressler et al. 2025; Lalakos et al. 2025), or by magnetohydrodynamic (MHD) instabilities, such as kink modes induced by interactions of the jet with its surroundings (e.g., Tchekhovskoy & Bromberg 2016; Bromberg & Tchekhovskoy 2016; Lalakos et al. 2024) and Kelvin–Helmholtz instabilities within the flow (e.g., Chow et al. 2023). Moreover, recent 3D MHD simulations showed that recollimation regions can trigger non-axisymmetric instabilities (e.g., kink modes), leading to jet distortion, enhanced dissipation, and quasi-periodic variability, with properties depending on the jet magnetization and external pressure profile (e.g., Boula et al. 2025; Hu et al. 2025). Finally, a binary supermassive black hole system has been proposed for 3C 279 (Qian et al. 2019), which might induce quasi-periodic jet orientation changes via orbital motion, spin–orbit coupling, or accretion-flow perturbations (e.g., Begelman et al. 1980; Ressler et al. 2025).

The source 3C 279 exhibits broadband emission extending from the radio band to VHE γ rays (Aleksić et al. 2011; H.E.S.S. Collaboration 2019), and the luminosity of the high-energy component generally dominates that of the synchrotron emission (Maraschi et al. 1994). High angular resolution (microarcsecond-scale) observations with RadioAstron resolved the 3C 279 jet, uncovering several filaments that were interpreted as the result of plasma instabilities in a kinetically dominated flow (Fuentes et al. 2023). The source varies strongly across the entire electromagnetic spectrum (e.g., Hayashida et al. 2012), and the γ-ray fluxes vary by more than two orders of magnitude, from $\sim 10^{-7}$ to $10^{-5}\,\mathrm{cm^{-2}\,s^{-1}}$ above 100 MeV (see, e.g., Ackermann et al. 2016). Multiwavelength (MWL) monitoring during a γ-ray flare in 2009 revealed a correlated change in optical polarization, providing evidence of a direct link between high-energy activity and the dynamics of the jet magnetic field (Abdo et al. 2010).

The source is known for intense and rapid γ-ray flaring activity. On June 16, 2015, the Large Area Telescope (LAT) on board the *Fermi Gamma-ray Space Telescope* detected a giant outburst with minute-scale variability, showing flux-doubling times shorter than 5 min (Ackermann et al. 2016). Such a rapid variability implies a very compact emission region, located at distances of a few hundred Schwarzschild radii from the central engine in conical jet models. During the same flare, VHE γ rays were detected with H.E.S.S., indicating an emission site at $r > 1.7 \times 10^{17}$ cm, that is, beyond the expected extent of the broad-line region (H.E.S.S. Collaboration 2019). Likewise, *Fermi*-LAT observations in April 2018 revealed a distinctive double-peaked γ-ray variability pattern on minute timescales, consistent with particle acceleration via relativistic magnetic reconnection. The absence of significant $\gamma\gamma$ absorption further constrains the emission region to $\sim 10^4$ gravitational radii, where turbulence is likely sustained by fluid-dynamical kink instabilities (Shukla & Mannheim 2020).

In analogy with the MWL campaigns accompanying the EHT observations of M87* (EHT MWL Science Working Group et al. 2021, 2024), coordinated quasi-simultaneous MWL observations of 3C 279 were conducted during the 2017 EHT observing run. This dataset provides a unique opportunity to investigate jet physics and particle acceleration processes, supports the interpretation and modeling of the EHT results, and constitutes a valuable legacy resource for the wider astronomical community.

The paper is structured as follows. In Sect. 2 we briefly describe the MWL observational campaign on 3C 279 accompanying the 2017 EHT observations, while further details on data processing and individual results are provided in Appendix B. In Sect. 3 we present the radio multifrequency jet structure, the MWL variability and quasi-simultaneous spectrum. In Sect. 4 we describe the phenomenological modeling using the turbulent extreme multi-zone (TEMZ) model. Sect. 5 discusses the jet structure and the origin of the γ-ray flaring activity. Finally, Sect. 6 summarizes our main results and conclusions.

2. Observations

As a main calibrator for EHT primary targets, 3C 279 was monitored during the first EHT observing campaign, conducted between April 5 and 11, 2017. Complementary MWL observations were performed in conjunction with the EHT runs, covering a broad frequency range, from 1.7 GHz with RadioAstron to VHE γ rays with the tHigh Energy Stereoscopic System (H.E.S.S.) and the The Major Atmospheric Gamma Imaging Cherenkov (MAGIC). Figure 1 summarizes the observational coverage between March and April 2017 during the first EHT–MWL campaign. In addition to the instruments shown in the figure, our analysis also incorporates cumulative flux estimates from RadioAstron at 1.7 and 5 GHz, spanning the period 2016–2018.

The following subsections provide brief descriptions of the individual observations carried out during the 2017 MWL campaign on 3C 279. Comprehensive details, including data-processing procedures and band-specific analyses and results, are presented in Appendix B.

2.1. Radio

The blazar 3C 279 was observed with several radio facilities in the centimeter (cm) and millimeter (mm) wavelength bands in VLBI and single-dish modes; details of the observations and data reduction are provided in Appendix B.1. High-resolution (milliarcsecond-scale) core monitoring of the source was carried out with the Very Long Baseline Array (VLBA) at 43 GHz and with the Korean VLBI Network (KVN) through multifrequency observations at 22, 43, 86, and 129 GHz. These data reveal variability in the core flux density, with the emission increasing during April–May (see Sect. 3.2). At millimeter wavelengths, the Submillimeter Array (SMA) and ALMA performed approximately weekly observations and also observed during EHT observations (Goddi et al. 2021), providing information on the more extended (arcsecond-scale) emission.

2.2. IR, optical, and UV

The source was monitored in the IR, optical, and UV range from 1220 nm with the Kanata telescope (see Appendix B.2.1) to 193 nm with *Swift*-UVOT (see Appendix B.2.3). Moreover, well-sampled optical polarimetric observations of 3C 279 in the *R* band, together with photometric measurements, were obtained with four telescopes: the 1.8 m Perkins Telescope, the 40 cm LX-200 telescope, the 70 cm AZT-8 telescope, and the 1.54 m Kuiper Telescope (see Appendix B.2.2 for details).

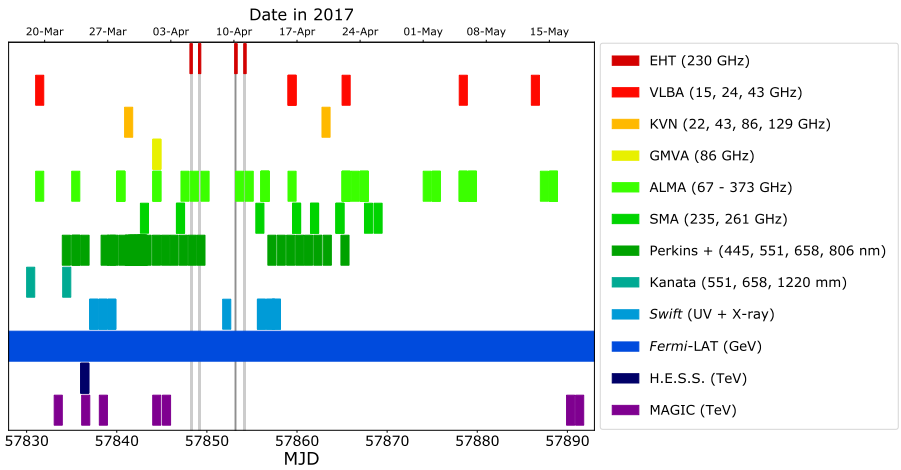


Fig. 1. Summary of the instrument coverage during the 2017 MWL campaign on the blazar 3C 279. The vertical gray bands refer to the EHT observations in the first row. The vertical dark gray line marks the date of the EHT observation we used for the spectral analysis.

2.3. X-rays and γ rays

In the X-ray band, 3C 279 was observed with *Swift*-XRT in the 0.3–10 keV energy range (see Appendix B.3). During the 2017 campaign, the source was monitored on March 26 and 27 and on April 8, 12, and 13, and all observations were performed in photon-counting mode.

Above 100 MeV, the *Fermi* Large Area Telescope (LAT) detected significant emission from 3C 279 on three-hour timescales (see also Appendix B.4.1). The source entered a high-activity state at the end of March, and the flaring episode ceased around April 9, shortly before the conclusion of the EHT observing window.

At VHE γ rays, the source was observed by H.E.S.S. and MAGIC (see Appendices B.4.2 and B.4.3 for details). H.E.S.S. conducted observations totaling 4.2 h during the night of 24–25 March 2017, following a bright-moon break and recorded optical flaring episodes of the source. No significant VHE emission was detected. Similarly, MAGIC accumulated 8.51 h of data between March and April 2017. 3C 279 was not detected above 5σ for individual nightly observations or during the stacked analysis for the entire observation campaign. The only data point shown in the MWL light curves (LC) (Fig. 4) together with the U.L.s corresponds to a 2.5σ fluctuation (the LC shows U.L.s below 2σ and data points otherwise).

3. Multiwavelength results

3.1. Radio structure

The radio morphology of the jet of 3C 279 (Fig. 2) consists of a compact core (the brightest region located in the northeast corner of the image) and an extended, nearly straight jet, visible up to deprojected scales of about 700 pc at 15 GHz, assuming a viewing angle of 1.5° (Larionov et al. 2020). Figure 2 presents a composite radio image of the jet structure of 3C 279 obtained in April 2017 from single-epoch VLBI observations at 15, 24, 43, 86, and 230 GHz, using the Very Long Baseline Array (VLBA), the Global Millimeter VLBI Array (GMVA), and the EHT. The accompanying VLBA 43 GHz observations were taken with a monthly cadence between February and June, 2017, enabling studies of the total and polarized intensity evolution.

At 230 GHz, the nuclear region is elongated nearly transversely to the direction of the larger-scale jet, separated from the other jet component by ~100 μas (~24 pc, deprojected). The apparent position angle of the inner jet smoothly changes from about −138° at 15 GHz to about −174° at 230 GHz. Figure 3 presents a sequence of multi-epoch 43 GHz VLBA images showing the evolution of the total and polarized intensity between February and June 2017. The parameters of these images are presented in Table 1. The images were obtained within the VLBA-BU-BLAZAR program. We used fully calibrated data posted at the program website[1] to construct the total and polarized intensity images shown in Figure 3 and to calculate the parameters listed in Table 1.

For the kinematics of 3C 279 at 43 GHz during the 2017 EHT campaign, we employed the results provided by Weaver et al. (2022). According to their analysis, a superluminal knot (component C37), detected for the first time in the jet around the end of October 2017, was ejected on April 2, 2017 (±13 days), from the center of the 43 GHz VLBI core with an apparent speed of $(25 \pm 2)\,c$, one of the highest apparent speeds of known components seen for this source. In the image of June 8, 2017, the knot should be ~0.14 mas from the center of the core, which is well inside the core region designated in Figure 3. The ejection appears to have triggered high total and polarized flux in the core region: the average flux density of the core region during the period from June 2007 to December 2018 is (8.5 ± 2.4) Jy Weaver et al. (2022), while the core flux density on June 8, 2017, is about 1.5 times higher than this value. This is accompanied by an elevated linear polarization degree of about 11%, which is a few times higher than the quiescent value (Larionov et al. 2020).

Table 1. Polarization parameters of the jet with the VLBA at 43 GHz.

Date[a]	MJD	$S_{\rm int}$[b]	$P_{\rm int}$[c]	$\chi_{\rm int}$[d]	$S_{\rm core}$[e]	$P_{\rm core}$[f]	$\chi_{\rm core}$[g]
		[Jy]	[%]	[°]	[Jy]	[%]	[°]
Feb. 4	57788	11.77 ± 0.59	9.7 ± 1.0	35 ± 6	8.66 ± 0.44	8.7 ± 0.9	40 ± 6
Mar. 19	57831	7.70 ± 0.39	10.7 ± 1.1	42 ± 6	6.14 ± 0.31	10.1 ± 1.0	47 ± 6
Apr. 16	57859	8.47 ± 0.43	11.1 ± 1.1	40 ± 5	7.05 ± 0.36	10.4 ± 1.1	43 ± 5
May 13	57886	12.69 ± 0.64	11.5 ± 1.2	50 ± 6	11.03 ± 0.55	11.0 ± 1.2	50 ± 7
Jun. 8	57912	14.76 ± 0.74	13.1 ± 1.3	35 ± 6	12.87 ± 0.65	11.3 ± 1.1	34 ± 6

Notes. [a] Epoch of observation. [b] Total intensity integrated over the image. [c] Degree of polarization integrated over the image. [d] Position angle of the polarization integrated over the image. [e] Total intensity of the core region designated in Figure 3. [f] Degree of polarization of the core region; uncertainties are given at the 1σ level. [g] Position angle of the polarization in the core region; uncertainties are given at the 1σ level.

[1] https://www.bu.edu/blazars/BEAM-ME.html

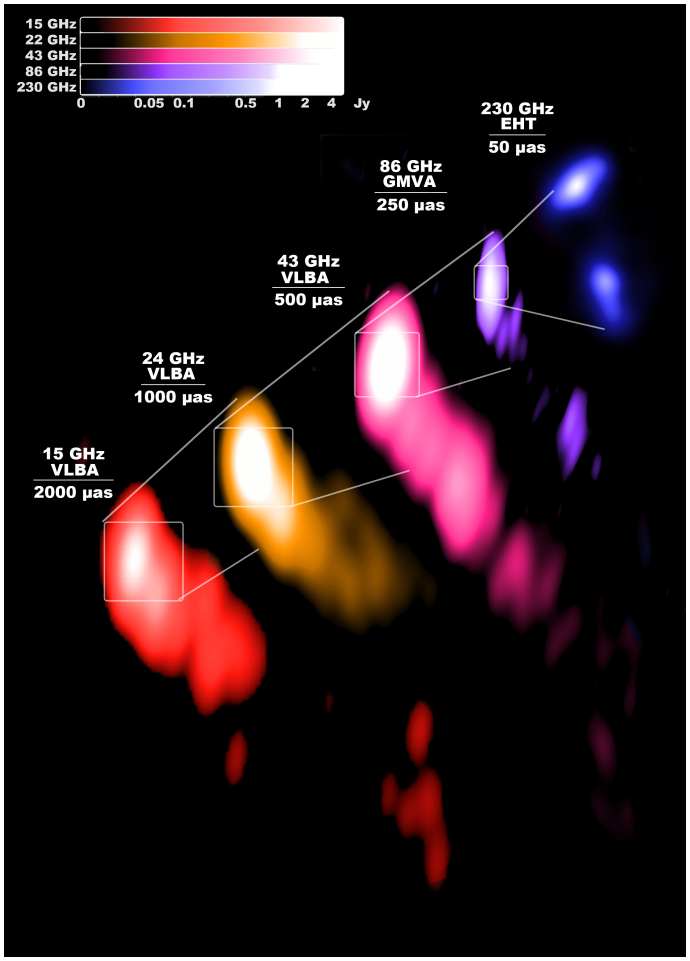


Fig. 2. Multifrequency (15, 24, 43, 86, and 230 GHz) composite radio image of 3C 279 obtained in April 2017.

3.2. Multiwavelength results and variability

Figure 4 presents the short-term (March–April 2017) MWL LC, including the polarization intensity (P) and electric vector position angle (EVPA) of 3C 279, obtained with the instruments participating in the coordinated EHT–MWL campaign.

The EHT observations of the innermost core region (component C0–0 in Kim et al. 2020) reveal a pronounced flux enhancement between April 5–6 and 10–11, with the core flux nearly doubling from ∼0.5 Jy to ∼0.95 Jy. During this period, the corresponding brightness temperature changed from approximately 6×10^{10} K to 4.5×10^{10} K. In contrast, the immediately adjacent components C0–1 and C0–2, located at projected separations of 15–30 μas (corresponding to ∼0.1–0.2 pc from the core) and exhibiting superluminal motion, show opposite trends: C0–1 displays a slight dimming, while C0–2 brightens. An increase in the core flux density F_ν is expected to be accompanied by a shift of the synchrotron self-absorption turnover frequency ν_m toward higher values. The scaling of ν_m with F_ν depends on whether the variability is driven by changes in the relativistic electron density normalization N_0, magnetic field strength B, or Doppler factor δ. Using Eqs. (1) and (2) of Marscher & Gear (1985),

$$F_\nu \propto N_0 B^{(s+1)/2} \delta^{(s+3)/2} \tag{1}$$

and

$$\nu_m \propto N_0^{2/(s+4)} B^{(s+2)/(s+4)} \delta^{(s+2)/(s+4)}, \tag{2}$$

where $-s$ is the slope of the electron energy distribution and the dimensions of the source are assumed to be constant, we can determine how ν_m is expected to vary when either N_0, B, or δ changes while the other parameters remain constant. In each case, we used relation (1) to solve for the variable parameter in terms of F_ν and the two constant parameters, and we then substituted that expression into expression (2) to obtain

$$\begin{aligned} \nu_m &\propto F_\nu^{2/(s+4)} && \text{(variation in } N_0\text{)}, \\ \nu_m &\propto F_\nu^{2(s+2)/[(s+1)(s+4)]} && \text{(variation in } B\text{)}, \\ \nu_m &\propto F_\nu^{2(s+2)/[(s+3)(s+4)]} && \text{(variation in } \delta\text{)}. \end{aligned} \tag{3}$$

These scalings are valid provided that the observing frequency is not already close to the synchrotron self-absorption turnover frequency, where the spectral shape becomes strongly affected by opacity effects. For the value derived from our modeling, $s = 2.4$, the corresponding exponents are 0.31, 0.40, and 0.25, implying an increase in ν_m by factors of approximately 1.2, 1.3, and 1.2, respectively, when the 230 GHz flux density increases by a factor of 1.9, as we observed.

At larger scales, and at centimeter and millimeter radio frequencies, no significant flux variability on daily timescales is observed. In contrast, the source exhibits unprecedented flaring activity in the UV–optical bands, peaking on March 21–22 and reaching the maximum in the I-band at 22:26 UTC on March 21, with a magnitude of 12.309 ± 0.002. The synchrotron flux increases by a factor of ∼20 relative to historical low states, reaching its highest level ever reported (Larionov et al. 2020), while over the one-month timescale considered here, the optical emission varied by approximately an order of magnitude. Moreover, this record optical flare occurred during the rising phase of a strong γ-ray flaring episode (see also Sect. B.4.1). The optical polarization also varies strongly, with the polarization degree ranging from 5% to 25% and the polarization angle varying between 20° and 80°. During the 2017 EHT campaign, the source was in a low X-ray emission state, with a 0.3–10 keV flux of $F_{0.3-10\,\mathrm{keV}} = (1.5 \pm 0.3) \times 10^{-11}$ erg cm^{-2} s^{-1} and a photon index of $\Gamma_X = 1.5 \pm 0.1$. This flux is slightly lower than the long-term Swift-XRT average measured over the 2006–2022 period, $F_{0.3-10\,\mathrm{keV}} = 1.93 \times 10^{-11}$ erg cm^{-2} s^{-1} (Thekkoth et al. 2023).

In the γ-ray band, 3C 279 underwent intense flaring episodes, with *Fermi*-LAT three-hour binned fluxes reaching up to ten times the long-term (16-year) average ($\phi_{E>100\,\mathrm{MeV}} = (6.32 \pm 0.03) \times 10^{-7}$ ph cm^{-2} s^{-1}). For reference, the integrated flux reported in the 4FGL-DR4 catalog is $\phi_{E>100\,\mathrm{MeV}} \sim 5 \times 10^{-7}$ ph cm^{-2} s^{-1} (Abdollahi et al. 2022). During the EHT observing window (April 5–11), the source exhibited an average γ-ray flux of $\phi_{E>100,\mathrm{MeV}} = (2.07 \pm 0.07) \times 10^{-6}$ ph cm^{-2} s^{-1}. The emission was even enhanced on April 5–6, reaching $\phi_{E>100,\mathrm{MeV}} = (2.90 \pm 0.12) \times 10^{-6}$ ph cm^{-2} s^{-1}, and it subsequently declined toward its typical level by around April 9, shortly before the end of the EHT observing campaign. At VHEs, no significant emission was detected by H.E.S.S. or MAGIC during this period.

During the first EHT observing window (April 5–6), we measured a fractional variability amplitude (following Vaughan et al. 2003) of $F_{\mathrm{var}} = (40 \pm 5)\%$ in the HE γ-ray light curve. The shortest flux–halving time derived from the Fermi-LAT data (using the method of Zhang et al. 1999) is $t_{1/2} \simeq (9.0 \pm 2.5)$ h. The largest variability amplitudes are observed in the optical bands, with $F_{\mathrm{var}} \sim 82\%$ in R and ∼86% in I. The minimum optical variability timescale, $T_2^{\mathrm{min}} = (0.59 \pm 0.03)$ d (∼(14 ± 1) h), is comparable to previous constraints.

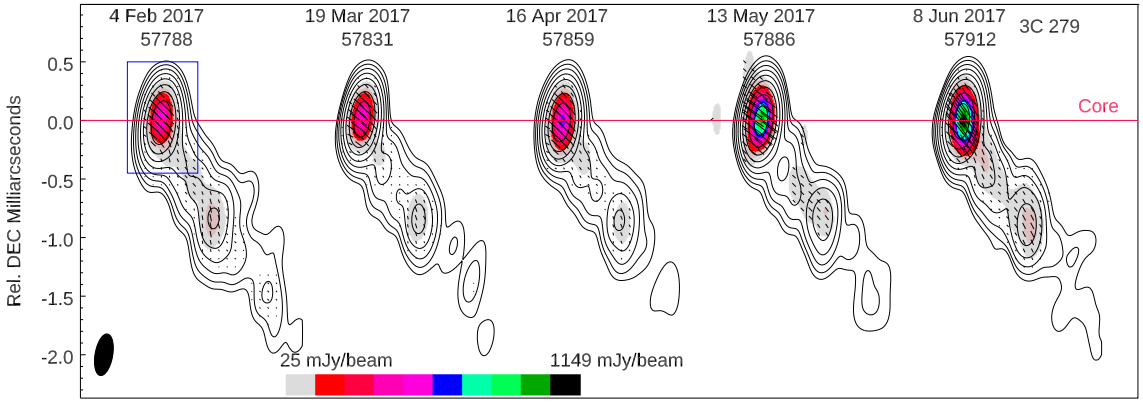


Fig. 3. Sequence of VLBA total (contours) and polarized (color scale) intensity images of 3C 279 at 43 GHz (magenta image in Fig. 2). The global intensity peak is 10.31 Jy/beam; the contour levels start at 0.25% of the peak and increase by factors of 2. All image parameters are listed in Table B.2. The images are convolved with the same beam of 0.36×0.15 mas^2 at PA = –10°(the ellipse in the bottom left corner); linear segments within the images indicate the direction of the electric vector position angle (direction of polarization). The blue rectangle in the first image shows the core region used to calculate the polarization parameters presented in Table 1.

While the *Fermi*-LAT light curve exhibits numerous short-timescale outbursts, the optical light curves display a broader peak and no clear counterpart to the rapid γ-ray activity. High optical fluxes occasionally coincide with high LAT fluxes, but the converse is not always true: comparable HE γ-ray fluxes may be observed during lower optical states, and a pronounced LAT flare occurred during an optical low state. A prolonged period of low emission is then observed in both bands. Overall, the Pearson correlation coefficient during the full period considered (see Fig. 4) is $r \sim 0$, and it remained modest ($r = 0.42 \pm 0.19$) up to MJD 57840, corresponding to the period of a simultaneous high state in the optical and γ-ray bands. Emery et al. (2019) reported a slight correlation between the HE γ-ray and optical fluxes ($r = 0.61 \pm 0.05$) when they restricted the analysis to MJD 57805–57840, immediately preceding our observing window, during which optical flares and increased HE γ-ray activity were detected. The same study found a much stronger correlation ($r \sim 0.9$) during the June 2018 optical and γ-ray flaring episode.

3.3. Multiwavelength spectrum

Figure 5 shows the quasi-simultaneous 2017 MWL broadband spectral energy distribution (SED) of 3C 279 obtained around the time of the EHT observations. To select the closest-in-time MWL data, the EHT observation on April 10 was used as a reference, since the only X-ray observation within the EHT window occurred on April 8. For the radio data included in the MWL SED, we considered the innermost region accessible at each observing frequency, corresponding to either the compact core alone (C0–0 component for the EHT data; see Kim et al. 2020) or, for non-EHT observations, to the combined emission from the core and the inner jet (see Table C.1). During the modeling phase (see Sect. 4), our first goal was to test whether the broadband emission (from radio up to γ rays) might originate predominantly from the central regions resolved by the EHT.

The SED exhibits the characteristic two-hump structure typical of blazars. The low-energy hump, produced by synchrotron emission, peaks in the IR–optical band, while the high-energy hump, attributed to inverse-Compton processes in most models (for a review, see Madejski & Sikora 2016), peaks in the γ-ray band at GeV energies. At this epoch, the source shows high Compton-dominance, with the high-energy component clearly dominating the low-energy synchrotron emission.

High-resolution VLBI observations spatially resolve the source structure, whereas at higher frequencies, the source appears to be point-like because the angular resolution is limited (see Sect. B.1). The SED also indicates the spatial scales corresponding to the total emission for the highest-resolution observations (for more information, see also Table C.1). All flux points correspond to statistically significant detections (>3σ) with 1σ uncertainties, except for upper limits, which are plotted at the 2σ confidence level.

4. Modeling the source emission

Visual inspection of Fig. 4 reveals a wide range of variability in the flux and linear polarization (degree and position angle) of 3C 279 at all observed wavelengths. There are no statistically significant trends in the individual light curves that persist on scales of months or years. A dedicated analysis will be presented in a forthcoming publication. This implies that stochastic processes play a major role in the emission. Furthermore, the position angles of optical and millimeter-wave polarization fluctuate by roughly ±20° about the jet direction. This requires substantial reconfiguration of the magnetic field pattern. This coexistence of ordered and turbulent magnetic field components can be produced by the superposition of a turbulent plasma embedded in a partially ordered magnetic field. The ordering can result from a helical magnetic field or from a chaotic field that is partially compressed when it crosses a shock.

4.1. The TEMZ model

Based on these considerations, we employed the Turbulent Extreme Multi-Zone[2] (TEMZ; Marscher 2014; Marscher et al. 2017; see also Zhang et al. 2023 and Liodakis et al. 2024) numerical model in an attempt to reproduce the time-variable broadband behavior and polarization of 3C 279. In this model, magnetized plasma flows at near light speed across a standing conical shock in a jet, as can occur where there is a mis-

[2] TEMZ is implemented via a Fortran-95 code and available at www.bu.edu/blazars/temz.html.

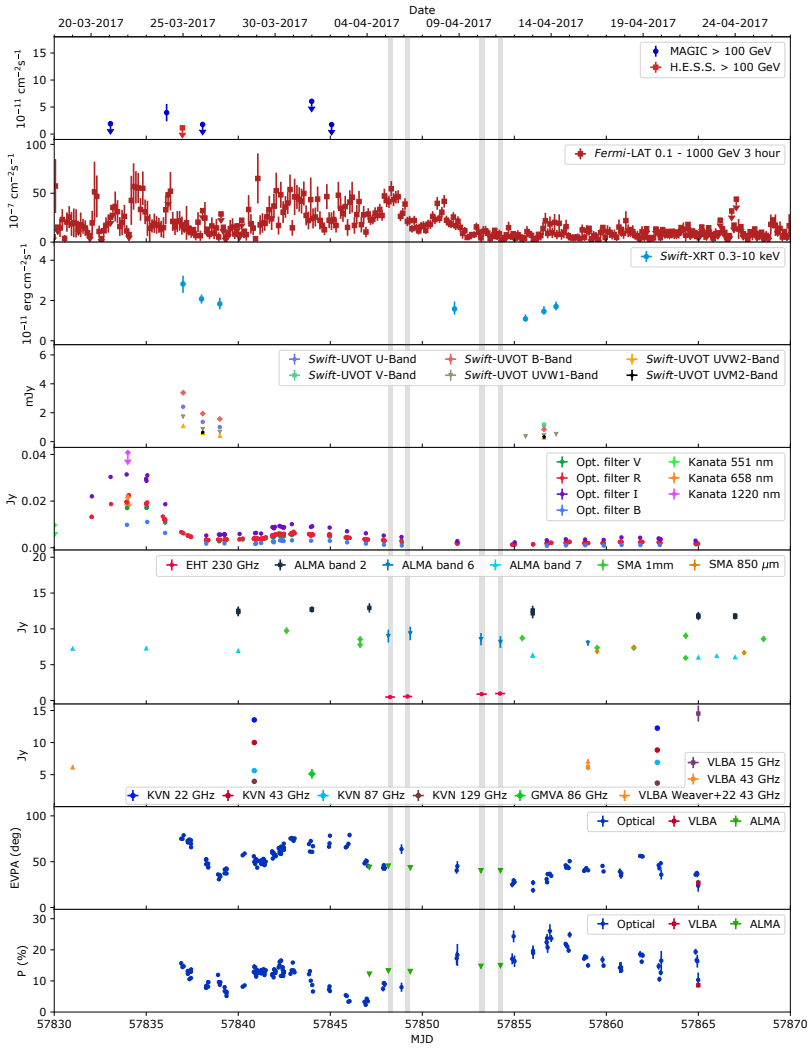


Fig. 4. MWL light curves of 3C 279 during MJD 57830–57870 (March 18–April 27, 2017). The gray bands indicate the periods of EHT observations. The top seven panels display the source flux, and the bottom two panels show the electric vector position angle and polarization intensity, respectively.

match between the internal and external pressure. We assumed that the upstream plasma consists of ultra-relativistic electrons and positrons, presumably energized via many minor magnetic reconnections and second-order Fermi acceleration, and colder protons (whose radiation was neglected here). The plasma was turbulent, although the magnetic field also included a helical component with opening angle ψ (whose extremes correspond to a toroidal field if $\psi = 90°$ and a longitudinal field if $\psi = 0°$). The shock compressed the component of the magnetic field that is perpendicular to the shock normal (as measured in the plasma frame), following the relativistic jump conditions (e.g., Königl 1980; Cawthorne & Cobb 1990). Diffusive shock acceleration increased the energies of the particles, forming a power-law energy distribution with a slope of $-s = -2.3$ up to a maximum energy $\gamma_{\rm max}mc^2$. At this energy, the acceleration and cooling times are equal for magnetic field directions that allow multiple back-and-forth passages of particles across the shock front (the "subluminal" regime; see Baring et al. 2017). To determine the acceleration time, we used the Baring et al. (2017) formulation, within which the mean-free path of pitch-angle scattering is proportional to the energy of the particle.

4.2. TEMZ implementation for 3C 279

We applied the TEMZ model by interpreting component C0–0 (EHT inner core) as a standing conical shock, located ∼1 pc from the supermassive black hole. The emission region extended from the shock front to a downstream rarefaction, as sketched in Figure 6. In order to reproduce the apparent superluminal motion of knots in 3C 279, observed to be as high as ∼40c in 2017 (Larionov et al. 2020), we set the bulk Lorentz factor of the flow to be 40[3] (the minimum value given the apparent speed) upstream of the shock, and the angle between the line of sight and jet axis to be 1.5°. This assumes no change in the flow speed between the high-energy emission region and the knots observed at 43 GHz. This requires that all of the bulk acceleration of the jet occurs upstream of component C0–0. We adopted an angle $\zeta = 6°$ between the shock front and the jet axis, which is inclined enough to allow substantial compression without decelerating the plasma flow too much (see Cawthorne & Cobb 1990).

The emission region contained a total of 2880 cylindrical cells, each with its own electron density, electron energy distribution, and unidirectional magnetic field. This number of cells reproduces the observed mean degree of optical polarization, which varies on a timescale of years over a range of ∼10–20% (Larionov et al. 2020). More turbulent cells would cause greater

[3] The bulk Lorentz factor needs to be high enough to attain the highest apparent speed observed during this period. While the Lorentz factor might increase downstream, the most rapid variability of 3C 279 (in the γ-ray band) also requires $\Gamma \sim 40$. A slightly wider or narrower viewing angle in C0 would cause the apparent speed there to be lower.

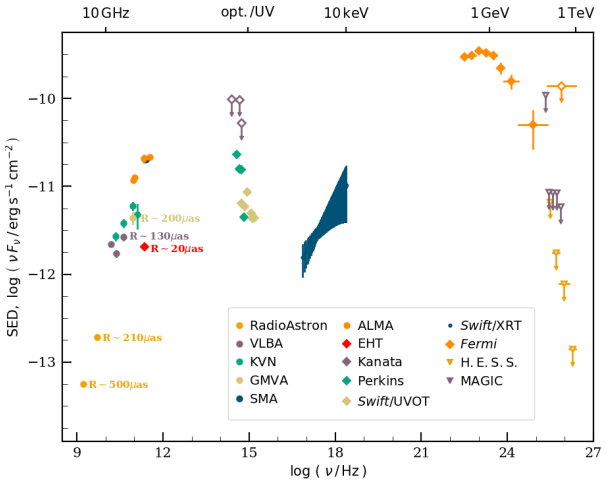


Fig. 5. MWL broadband SED of 3C 279 around the EHT observational campaign (MJD 57836–57861; see Table C.1 in Appendix C). For RadioAstron, integrated fluxes from cumulative observations between 2016 and 2018 are shown. The Swift-XRT spectrum is shown as a bow tie. The fluxes are indicated with different colors and markers according to the instrument. For radio VLBI and interferometric data, upper limits on the emission size (radius) at selected frequencies are labeled.

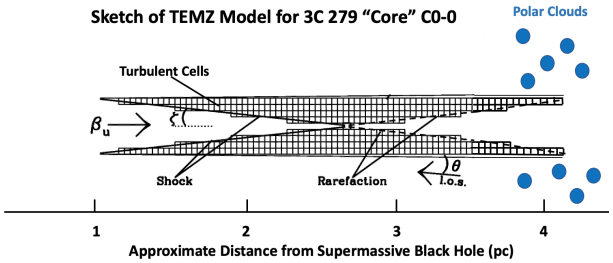


Fig. 6. Sketch of the TEMZ model for 3C 279 adapted from Marscher (2014). The emission region, ranging from the shock to the rarefaction, comprises 2880 turbulent cells. The line of sight (l.o.s) is inclined by angle θ to the jet axis.

cancellation of randomly unaligned polarization vectors. Each cell had a diameter of $\ell = 0.04$ pc and a length of $\Delta z = 0.048$ pc, the latter value chosen so that the upstream end of each ring of columns was offset by an integer (eight) number of cell lengths (see Fig. 6). The magnetic field included a helical and a turbulent component. The latter was assigned via a random number generator and was related to the turbulent field component of nearby cells via the relativistic Kolmogorov spectrum. This relation was accomplished in the manner of Jones (1988): each cell belonged to four zones: its own, one zone containing 8 ($2 \times 2 \times 2$) cells, another zone with 64 ($4 \times 4 \times 4$) cells, and one zone with 512 ($8 \times 8 \times 8$) cells.

The code selects the magnitude of the magnetic field, density and the direction of the field, randomly in each zone from a log-normal distribution. The field and density of a cell are then computed as the average of the values in its zones, weighted according to the Kolmogorov spectrum: weight $w \propto \ell^{2/3}$ for density, magnetic energy density, and square of the turbulent four-velocity. This weighting causes the larger zones to contribute a larger fraction of each quantity. In order to approximate the rotation of turbulent vortices, the code relativistically adds a turbulent circular four-velocity of $0.1c$, rotating about the center of each zone, to the systemic flow velocity (see Calafut & Wiita 2015).

We assumed that the electrons (including any positrons) at the upstream boundary of the emission region (i.e., just beyond the shock front) had a power-law energy distribution between a minimum energy $\gamma_{\rm min}mc^2$ and maximum energy $\gamma_{\rm max}mc^2$, the latter of which depends on the angle of the magnetic field relative to the shock normal as measured in the plasma frame (see above). This dependence of $\gamma_{\rm max}$ on the magnetic field direction, and the higher radiative energy losses of the higher-energy electrons as the plasma flows downstream of the shock front, means that the electron energies of only a fraction of the cells are high enough to produce synchrotron and Compton radiation at the highest frequencies. These effects cause the slope of the synchrotron and Compton spectra to steepen with frequency, so that, for example, the optical spectrum is steeper than that at infrared frequencies. The combination of the two effects causes the mean polarization and its level of variability to increase with frequency, as has been observed at X-ray and optical frequencies in several blazars (e.g., Liodakis et al. 2022; Marscher et al. 2024; MAGIC Collaboration 2025).

As the code runs, the plasma advances by one cell length Δz per time step. New values of the magnetic field and electron density are introduced at the upstream boundary. These values are derived from the turbulence simulation scheme discussed above, which produces short-term fluctuations, then multiplied by a time-dependent input of total energy density. The latter, which corresponds to variations in the energy injected into the base of the jet, is computed from random sampling of a power spectral density (PSD) in the form of a power law with a slope of -2, the value of which is consistent with the optical and X-ray timing analysis of 3C 279 by Chatterjee et al. (2008). To apply this, we adapted a subroutine supplied by R. Chatterjee, based on the algorithm of Timmer & König (1995), which produces a large set of random values x_i between -1 and 1 with a power-law PSD. Following Uttley et al. (2005), the TEMZ code exponentiates each number produced by the subroutine in order to derive a multiplicative factor $\exp(\xi x_i)$ that the code applies to the input value of the energy density, where ξ is a free parameter of the order of unity that determines the ratio of the highest to lowest flux density over time ranges of years. The ratio is observed to be ~100 in the case of the optical variability of 3C 279 (Larionov et al. 2020). During the time span of the observations reported here, the range was about one order of magnitude (see Fig. 4).

In the version of the TEMZ code we used for this work, the magnetic field and relativistic electron density of a cell remained constant as the plasma advanced downstream from the shock. However, the energy distribution of the electrons evolved toward lower energies with distance from the shock as they lost energy to synchrotron and Compton radiation (see Equations (5) and (6) of Marscher 2014). The energy-loss rate varied from one cell to the next, commensurate with the differences in the magnetic field and seed photon field among the cells. Adiabatic energy losses were neglected because the jet did not spread appreciably over the length of the computational grid.

The TEMZ code computes the flux density from incoherent synchrotron (including synchrotron self-absorption), synchrotron self-Compton (SSC), and external Compton (EC) radiation. The relevant formulas are given in Marscher (2014). The main difference of the model for 3C 279 from the earlier TEMZ versions is that the seed photons for SSC emission produced by a particular cell are from all of the other cells (instead of a Mach disk). The seed photon flux from other cells is suitably time-delayed and Doppler shifted, the latter of which takes into account variations in the turbulent velocities of the different cells. In addition, the seed photons for EC scattering are from a torus containing hot (1200 K) dust and from broad

emission-line clouds. For the latter, we used the prescription of Tavecchio & Ghisellini (2008), approximating the spectrum of the clouds as a blackbody with a temperature of 42 000 K.

The peak of the γ-ray SED of 3C 279 (Fig. 5) is an order of magnitude higher than that of the IR synchrotron emission, and it reached maximum at an energy of ∼1 GeV. These properties are difficult to reproduce with synchrotron seed photons from the jet (Sikora et al. 2009). Compton scattering of photons from the dust torus results in an SED peaking in the 0.01–0.1 GeV region in a blazar such as 3C 279 (Sikora et al. 2009), which is also inadequate. The canonical broad emission line region (BLR) is expected to consist of clouds in a shell or torus with an outer boundary $\lesssim$0.2 pc from the SMBH (see Tavecchio & Mazin 2009, for a discussion). Liu et al. (2008) showed that γ rays observed with energies $\gtrsim$30 GeV would be heavily depleted by pair production if they were emitted inside such a small dense BLR.

There is, however, another potential source of seed photons for Compton scattering to produce the γ rays: polar line-emitting clouds that lie along the outer boundary of the parsec-scale jet. Such clouds have been inferred from emission-line variability in 3C 279 (Larionov et al. 2020) and 4C29.45 (Hallum et al. 2022). A variable component of the Mg II line is on the red side of the main line, which implies that it is from clouds falling toward the SMBH, possibly as part of a back-flow surrounding the jet (Hallum et al. 2022). The line flux in both objects is proportional to the (beamed) optical flux from the jet, which indicates that the clouds lie along the jet. Since flares are short lived, we adopted a luminosity of the Mg II line from polar clouds in the low range reported by Larionov et al. (2020) and multiplied this by a factor of ∼10 to estimate the luminosity of all lines and continuum (see Peterson 1997) from the polar clouds to be $\sim 7 \times 10^{43}$ erg s^{-1}. We further adopted a distance of the clouds from the SMBH of ∼4 pc and a distance from the jet axis of ∼0.3 pc, which is somewhat smaller than the values estimated for the more luminous quasar 4C29.45 by Hallum et al. (2022).

The code calculates the pair-production opacity of VHE γ rays as they encounter photons from the line-emitting clouds and the extragalactic background light. These two sources of opacity to γ rays dominate in the model. The integrated (over solid angle) intensity of the optical-UV radiation from the clouds is calculated as a function of frequency at the position of every cell. The intensity times the frequency-dependent cross-section (Coppi & Blandford 1990) is integrated over optical-UV frequency to obtain the pair-production optical depth at each VHE energy. This is added to the optical depth from the extragalactic background light as determined by Domínguez et al. (2011). A number of input parameters of the code can be set based on observational information. Table 2 lists these parameters and their values. The mean kinetic power of the simulated jet is $\sim 7 \times 10^{46}$ erg s^{-1} if there are about as many protons as electrons in the jet. If positrons are the main positively-charged component, this is reduced by a factor of ∼2.

4.3. Model results

We ran a small number of sample computations of the TEMZ code in order to find values of the free parameters that produced flux, polarization, and SED versus time that roughly resembled the observed behavior of 3C 279. Table 2 describes these parameters and gives their adopted values.

After setting the above parameters based on the results of the trial runs, we ran the code for 10 000 time steps in order to produce the simulated flux, polarization, and SED at each step to compare them with the data. Because of the randomness inherent in the code (and in some of the actual physical processes), TEMZ cannot reproduce the actual flux and polarization curves. Instead, a successful simulation was one in which the above variations resembled the observed behavior. Since the observations have many temporal gaps, the comparison can only be made rather crudely: the mean and standard deviation of the degree and position angle of optical polarization, range of flux variations during a given time interval at different wavebands, and single-epoch SEDs.

Figure 7 shows the simulated light curves of flux and polarization as a function of time. The simulated fluxes span approximately one order of magnitude, consistent with the variability

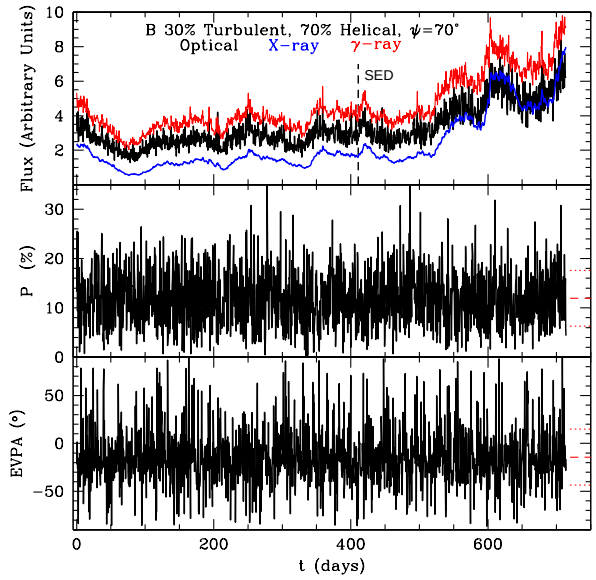


Fig. 7. Sample simulated MWL flux and optical polarization degree P and EVPA vs. time calculated with the TEMZ model. EVPA = 0° in the simulation corresponds to the jet direction. The time step corresponding to the SED presented in Fig. 8 is marked in the top panel. The means of P and the EVPA are indicated with dashed lines on the right of the respective panels, while the standard deviations are marked with dotted lines.

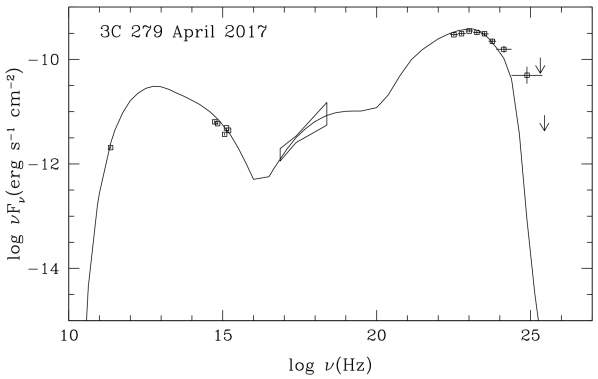


Fig. 8. Spectral energy distribution of 3C 279 in April 2017 (empty squares). Under the assumption that the high-energy emission arises from the core region (C0–0 in the EHT images), only EHT, Swift-UVOT, X-ray, and γ-ray spectral points are shown. Lower-resolution radio and optical data are excluded as they sample larger emission regions. The solid curve shows a representative SED of component C0-0 from the TEMZ model, selected at the epoch when the simulation reproduced the observed multiwavelength data best (see Fig. 7).

Table 2. Parameters of TEMZ Model for 3C 279.

Parameters based on observations		
Parameter	Value	Description
$v_{\rm lam}$	$0.9997c$	Bulk flow velocity of laminar component of the jet flow (Lorentz factor = 40.8)
θ	1.5°	Angle between jet axis and line of sight (set such that values of $v_{\rm lam}$ and θ result in apparent speed of $37c$ as observed in 2017 in Larionov et al. 2020)
$v_{\rm turb}$	$0.1c$	4-velocity of turbulent rotational component of the jet flow (see Calafut & Wiita 2015)
s	2.4	Slope of electron power-law energy distribution immediately past the shock front
ℓ	0.04 pc	Transverse diameter of a cell
Δz	0.048 pc	Length of a cell
ϕ	0.9°	Intrinsic opening half-angle of jet (Weaver et al. 2022)
–	7×10^{43} erg s^{-1}	Luminosity of thermal emission from polar clouds
–	4 pc	Mean distance of polar clouds from SMBH
–	0.3 pc	Mean distance of polar clouds from jet axis
Parameters based on modelling		
Parameter	Value	Description
σ_B,σ_n	0.3	Dispersion-to-mean ratio of turbulent fluctuations in magnetic energy and electron densities
ξ	1.2	Parameter in the exponent of the modulation of the input energy
$\langle B \rangle$	0.03 G	Mean value of magnetic field immediately upstream of shock
u_e/u_B	8	Mean ratio of relativistic electron to magnetic energy densities immediately upstream of shock
$N_{\rm cells}$	2880	Total number of computational cells
$E_{\rm max,min}$	$2 \times 10^5\, mc^2$	Highest value of maximum electron energy after plasma crosses shock
$E_{\rm max,max}$	$1 \times 10^4\, mc^2$	Lowest value of maximum electron energy after plasma crosses shock
$E_{\rm min}$	$800\, mc^2$	Minimum electron energy after plasma crosses shock
$\langle B_{\rm ord}/B_{\rm tot} \rangle$	0.3	Mean ratio of ordered helical to total (helical+turbulent) magnetic field
ψ	70°	Pitch angle of helical magnetic field

observed in 3C 279 (see Fig. 4). The mean optical EVPA differs only slightly from the jet direction (by 13°) and exhibits a standard deviation of 27°, comparable to the observational data. (The mean EVPA would align exactly with the jet axis if $\psi = 90°$.) The mean degree of polarization in the simulation is 12%, with a standard deviation of 6%. These simulated values agree well with the observations, which yield a mean polarization degree of (14 ± 5)% and a mean optical EVPA of $(46.5 \pm 13.9)°$, derived from the observational data binned in two-day intervals.

Figure 8 displays the simulated SED of component C0–0 at a time when the simulation most closely resembled the data. The radio to optical portion is from synchrotron radiation, while SSC emission dominates the X-ray flux. The γ-ray emission is mainly external Compton of emission-line photons from the polar clouds. The polar clouds contribute to the optical-UV emission lines and to a relatively weak thermal continuum component in the optical–UV range.

5. Discussion

5.1. Jet structure

Microarcsecond-scale angular resolution observations of 3C 279 with RadioAstron on March 10, 2014, resolved the jet transversely, revealing multiple filaments that were likely produced by plasma instabilities within a kinetically dominated flow (Fuentes et al. 2023). Due to the sparse sampling of the Fourier plane, the 2017 EHT observations (Kim et al. 2020) were only able to recover one central filament, shown in Fig. 2 as a separated extended jet, which was oriented perpendicularly to the elongated nuclear region. On the other hand, our VLBI observations at longer wavelengths do not resolve the filamentary jet structure at all. Fuentes et al. (2023) suggested that enhanced Doppler boosting might occur when emitting regions traverse such sites where the local jet direction becomes more closely aligned with the line of sight, leading to the observed flux variability. Fuentes et al. (2023) concluded that resolved bright filaments of the jet of 3C 279 represent compressed regions with enhanced gas and magnetic pressure and might be associated with the triggering and development of flow instabilities. Current-driven kink or Kelvin–Helmholtz instabilities are the most plausible mechanisms for developing such helical structures. On the other hand, the elongated complex nuclear structure at 230 GHz might originate from an extreme bend of the jet.

More recent RadioAstron observations obtained in January 2018 similarly revealed fine-scale structure within the relativistic jet, extending up to a projected distance of approximately 180 pc from the radio core (Toscano et al. 2025). Although no filamentary features were detected in these later observations, this might be due to the substantial decline in the total jet intensity and the limited uv coverage. The data further suggest a predominantly toroidal magnetic field configuration, consistent with an overall helical magnetic structure. Independent constraints from multiwavelength variability provide a complementary picture. The behavior of the optical and radio (including 43 GHz) Stokes parameters (Larionov et al. 2020) is also compatible with a predominantly helical magnetic field configuration, or alternatively, with radiating plasma moving on a spiral trajectory.

Recently, Kravchenko et al. (2025) used 15.4 GHz multi-epoch monitoring data to analyze the dependence of the jet component size, r, on the distance from the VLBI core, d, for a sample of 447 AGN jets. They concluded that the size of the jet components is a good tracer of jet geometry. Particularly for 3C 279, Kravchenko et al. (2025) obtained the dependence $d \propto r^{0.92\pm0.1}$, which implies that the blazar jet follows a conically expanding streamline at scales ~0.2–2.4 mas (~7–90 pc deprojected with $\theta = 1.5°$). This result is consistent with the

estimates of the spatial extension of the intrinsic jet acceleration zone, which are that this zone lies within 100 μas from the core (∼25 pc deprojected) (Kim et al. 2020).

Using the 2016–2018 short-segment observations of 3C 279 at 18 cm and 6 cm with RadioAstron (see Sect. B.1.1), we fitted the measured visibility amplitudes with three Gaussian components: the largest component, which represented the extended jet; the VLBI core; and a substructure within the core. The latter exhibits a high observed brightness temperature of $T_b \sim 10^{13}$ K, exceeding that of the core itself. This suggests the presence of more energetic particles in the region. In the TEMZ scenario of the turbulent plasma crossing a shock, and given the Doppler factor > 30, the rest-frame brightness temperature of a single cell is then $T_b \sim 3 \times 10^{11}$ K. This indicates that any of the compact turbulent cells could have such a high T_b at cm wavelengths.

From the 2017 EHT observations, Kim et al. (2020) observed significant day-to-day variations in the closure phases, which appear to be most pronounced in the triangles with the longest baselines. These authors showed that this variation is related to a systematic change in the source structure, which is accompanied by rapid changes in the brightness temperature within the subnuclear structure of the 3C 279 jet over the time interval of a week. Two inner jet components move non-radially at apparent speeds of ∼15 c and ∼20 c, which more strongly supports the scenario of traveling shocks or instabilities in a bent, possibly rotating jet.

The components in the jet of 3C 279 are known to exhibit significantly different speeds and position angles (Jorstad et al. 2004; Weaver et al. 2022), which have been interpreted as evidence of a precessing jet (Abraham & Carrara 1998). Jet-nozzle precession models suggest that the components follow a curved precessing path with a period of ∼25 yr (Qian 2011, 2012). However, EHT observations (Kim et al. 2020) revealed erratic changes in the inner jet position angle in 2011 and 2017, implying a precession period <6 yr if periodic. Shorter-scale quasi-periodic variations of ∼3 yr have also been reported (Lister et al. 2021). Observations at 1.3 mm in 2011 indicate dthat the inner jet orientation does not fully match precession-model predictions, suggesting an additional erratic process (Lu et al. 2013). A light-curve analysis across radio, optical, and X-ray bands found a period of $P = 130.6 \pm 1.3$ days (Li et al. 2009). Long-term PA changes (>10 yr) might still be governed by jet-nozzle precession, consistent with the ∼39° smooth shift observed between extended radio jet regions (Fig. 2). In contrast, shorter-term variations are likely produced by MHD instabilities in disk-jet systems, as suggested by recent 3D MHD simulations (Hu et al. 2025).

Similar multi-period jet position angle variations have been observed in M87 (Ro et al. 2026; Cui et al. 2023), with an 11 yr period consistent with Lense–Thirring precession from a tilted accretion disk (Cui et al. 2023). Shorter ∼1 yr transverse oscillations (Ro et al. 2026) might result from transverse MHD waves (excited by precession, nutation, or magnetic flux eruptions near the central engine) or from jet instabilities such as current-driven or Kelvin–Helmholtz modes. Evidence of the latter has been recently reported within the Bondi radius, revealing helical and elliptical surface modes (Nikonov et al. 2023; Kravchenko et al. 2026). Substantial evidence exists of periodic position-angle variations in other AGN jets (e.g., Kostrichkin et al. 2025; Lisakov et al. 2025). Moreover, precessing-jet models successfully reproduce the complex linear polarization profiles observed in AGN jets (Todorov et al. 2023), which are inconsistent with simple magnetic field configurations (Pushkarev et al. 2023).

5.2. Origin of the γ-ray flaring activity

As discussed in Sect. 4, the observed spectral and polarization variability can be interpreted within a turbulent plasma jet model. In this framework, turbulent cells crossing a stationary conical shock are compressed, which triggers rapid γ-ray flares and produces polarization variability, including EVPA rotations and increases in polarized intensity. Our TEMZ simulations reproduced flux variations of roughly one order of magnitude, mean optical polarization degrees of 12% ($\sigma \approx 6\%$), and EVPA deviations of 13° from the jet axis with ∼27°, consistent with the observed values of 14 ± 5% and 46.5 ± 13.9°, see Fig. 4.

Magnetic reconnection near the collimation zone provides an additional dissipation mechanism (Shukla & Mannheim 2020), where kink or shear-flow instabilities create filamentary structures that efficiently convert magnetic energy. Relativistic particles accelerated in these sites can produce γ-rays via inverse Compton scattering. For typical fields $B \sim 0.1-1$ G and bulk Lorentz factors $\Gamma \sim 20$, this process reproduces the observed γ-ray fluxes and one- to two-day timescales, while higher magnetic fields and Lorentz factors can produce even shorter flares (e.g., Giannios 2013; Petropoulou et al. 2016).

Further constraints on the high-energy emission mechanism come from more recent IXPE observations of 3C 279 (Marshall et al. 2024). The X-ray spectrum was fitted with a power law ($\Gamma = 1.79 \pm 0.04$) and Galactic absorption of $N_H = 2.25 \times 10^{20}$ cm^{-2}. The X-ray polarization degree was constrained to be <12.7%, compared to ∼4% in the millimeter and ∼12% in the optical and IR bands. While the current IXPE constraint does not by itself rule out a hadronic origin of the X-rays, it is compatible with leptonic models in which the X-ray and γ-ray emission is dominated by inverse-Compton scattering of synchrotron or external photons by relativistic electrons in the jet. Similarly, during a TeV flare of the blazar Mrk 421 observed jointly with IXPE, strong and erratic X-ray polarization variability was detected, while the optical polarization remained nearly constant (MAGIC Collaboration 2025). This behavior closely resembles the γ-ray flaring state of 3C 279 in April 2017, albeit at higher energies given the high-synchrotron-peak nature of Mrk 421 compared to the low-synchrotron-peak classification of 3C 279. In contrast, the flare in 3C 279 is more pronounced in the MeV–GeV band, and the polarization variability is observed in the optical.

The kinematic analysis by Weaver et al. (2022) indicated that a superluminal knot (C37) was ejected at $T_0 = 2017.253 \pm 0.035$ (April 2 ± 13 days) with an apparent velocity of $(25 \pm 2)c$, coinciding with γ-ray flaring activity in late March – early April (Fig. 4). The optical peak at the end of March, along with enhanced γ-ray flux, likely reflects an increase in the magnetic field strength and radiating electron density (Larionov et al. 2020). A concurrent rise in the radio-core polarization was observed in April–May 2017 (Fig. 3). These observations are consistent with a shock-in-jet scenario, where a disturbance near the jet base propagates downstream, becoming a superluminal radio knot. The high apparent speed of C37 suggests either an increase in the bulk Lorentz factor Γ or a change in jet orientation (Larionov et al. 2020). Doppler factor variations, coupled with changes in the emitting electron population, are consistent with emission modeling of previous flares (Hayashida et al. 2015; Larionov et al. 2020; Mohana et al. 2025).

Finally, the unprecedented optical flare (a synchrotron flux increase of ∼20× above the low state), together with contemporaneous UV and X-ray enhancements observed by Swift during the onset of the γ-ray flare (see Fig. 4), supports a

cospatial origin of the emission across these bands. Flux variability is likely driven by knot evolution and structural changes in the jet. This interpretation is consistent with the simultaneous γ-ray flare and optical polarization event reported by Abdo et al. (2010) and with zero-lag optical-UV–γ-ray correlations observed during flares (Rani et al. 2017; Prince 2020).

6. Summary

We presented the results of the first MWL observational campaign on 3C 279 together with the highest ever resolution millimeter-VLBI images using the EHT from its April 2017 campaign. This includes one of the most extensive quasi-simultaneous broadband spectra, along with details of the individual observations and light curves aimed at investigating its emission variability and constraining the origin of the γ-ray emission in this source. The primary outcome of this campaign is represented by the rich legacy dataset, for which all data and some analysis scripts are available to the community via a CYVERSE repository (see Appendix C). While we defer a detailed modeling to future works by the broader community, we draw preliminary conclusions using a heuristic approach to the SED modeling.

The main results of the 2017 EHT–MWL observational campaign on 3C 279 can be summarised as follows:

- EHT observations of the innermost core region (component C0–0; Kim et al. 2020) reveal a clear flux increase from ∼0.5 Jy to ∼0.95 Jy between April 5–6 and 10–11.
- VLBA observations reveal a significant enhancement of the core flux density and polarized emission during April–May. Weaver et al. (2022) reported the contemporaneous ejection of a superluminal knot at $T_0 = 2017.253 \pm 0.035$ (April 2 ± 13 days), presenting a high apparent speed of (25 ± 2) c.
- An unprecedented UV–optical flare, with synchrotron flux increases by a factor of ∼20 relative to the low state, was detected around March 21–22, followed by a low-emission state in April. Strong optical polarization variability (degree 5–25%, angle 20°–80°) closely followed the optical flux evolution.
- In the X-ray band, *Swift*-XRT observations indicate a low X-ray emission state, with a flux below the long-term average.
- High-energy γ-ray flaring activity was observed between late March and early April. It ceased before the end of the EHT observing window, while no significant VHE emission was detected.
- The broadband variability in the SED and polarization can be reproduced with a jet model involving turbulent plasma, as simulated using the TEMZ code (see Sect. 4). In this scenario, turbulent cells crossing a stationary conical shock undergo compression capable of triggering the observed γ-ray flares.
- The high observed brightness temperature of $T_b \sim 10^{13}$ K obtained from the RadioAstron observations at 18 cm and 6 cm supports the TEMZ scenario and existence of the compact components in the 3C 279 jet.
- An alternative scenario suggested by the observations is that the γ-ray flare might be associated with a moving shock-in-jet, possibly linked to the superluminal component ejected during the same period.

The results of this broadband MWL campaign on 3C 279 provide a valuable opportunity to probe the origin of the γ-ray emission during a γ-ray flaring episode. They underscore the crucial role of coordinated densely sampled MWL observations in capturing and characterizing the spectral variability of 3C 279, which likely spans multiple temporal scales. Furthermore, the publicly released datasets from this campaign constitute a rich resource for future studies.

The EHT–MWL observational campaigns conducted with increasingly sensitive arrays in 2018, 2021, 2022, 2024, 2025, and those planned for the coming years, will provide crucial new insights into the physical processes at play in the archetypal blazar 3C 279. They include improved constraints on the jet structure and the origin and mechanisms that produce γ-ray emission. The synergy between high-resolution EHT mm-VLBI imaging and broadband SED information will enable a deeper understanding of the emission mechanisms that power AGNs.

Data availability

Data products presented in this paper are available for download through the EHT Collaboration Data Webpage (`https://eventhorizontelescope.org/for-astronomers/data`), or *Fermi*-LAT Collaboration Publication Webpage (`https://www-glast.stanford.edu/cgi-bin/pubpub`). The repository contains the following data products:

- Broadband spectrum table (see Table C.1) with frequency, flux density, its uncertainty, and instrument index (format: DAT).
- Multi-wavelength light curve (see Fig. 4) table with frequency, flux density, its uncertainty, and instrument index (format: DAT).
- Sampled posterior distributions of the SED broadband spectral model described in Sect. 4 (format:DAT).

Acknowledgements. The full acknowledgements are available in Appendix A.

References

Abdo, A. A., Ackermann, M., Ajello, M., et al. 2009, Phys. Rev. D, 80, 122004
Abdo, A. A., Ackermann, M., Ajello, M., et al. 2010, Nature, 463, 919
Abdollahi, S., Acero, F., Ackermann, M., et al. 2020, ApJS, 247, 33
Abdollahi, S., Acero, F., Baldini, L., et al. 2022, ApJS, 260, 53
Abraham, Z., & Carrara, E. A. 1998, ApJ, 496, 172
Ackermann, M., Anantua, R., Asano, K., et al. 2016, ApJ, 824, L20
Aharonian, F., Akhperjanian, A. G., Bazer-Bachi, A. R., et al. 2006, A&A, 457, 899
Ajello, M., Angioni, R., Axelsson, M., et al. 2020, ApJ, 892, 105
Akitaya, H., Moritani, Y., Ui, T., et al. 2014, SPIE Conf. Ser., 9147, 91474O
Aleksić, J., Antonelli, L. A., Antoranz, P., et al. 2011, A&A, 530, A4
Aleksić, J., Ansoldi, S., Antonelli, L. A., et al. 2016, Astropart. Phys., 72, 76
Angelakis, E., Hovatta, T., Blinov, D., et al. 2016, MNRAS, 463, 3365
Baring, M. G., Böttcher, M., & Summerlin, E. J. 2017, MNRAS, 464, 4875
Begelman, M. C., Blandford, R. D., & Rees, M. J. 1980, Nature, 287, 307
Berge, D., Funk, S., & Hinton, J. 2007, A&A, 466, 1219
Bertin, E., & Arnouts, S. 1996, A&AS, 117, 393
Blandford, R., Meier, D., & Readhead, A. 2019, ARA&A, 57, 467
Boula, S., Tavecchio, F., Bodo, G., et al. 2025, A&A, 704, A200
Breeveld, A. A., Landsman, W., Holland, S. T., et al. 2011, AIP Conf. Ser., 1358, 373
Bromberg, O., & Tchekhovskoy, A. 2016, MNRAS, 456, 1739
Bruel, P., Burnett, T. H., Digel, S. W., et al. 2018, arXiv e-prints [arXiv:1810.11394]
Burrows, D. N., Hill, J. E., Nousek, J. A., et al. 2005, Space Sci. Rev., 120, 165
Calafut, V., & Wiita, P. J. 2015, JApA, 36, 255
Cash, W. 1979, ApJ, 228, 939
Cawthorne, T. V., & Cobb, W. K. 1990, ApJ, 350, 536
Chatterjee, R., Jorstad, S. G., Marscher, A. P., et al. 2008, ApJ, 689, 79
Chow, A., Davelaar, J., Rowan, M. E., & Sironi, L. 2023, ApJ, 951, L23
Coppi, P. S., & Blandford, R. D. 1990, MNRAS, 245, 453
Cui, Y., Hada, K., Kawashima, T., et al. 2023, Nature, 621, 711
de Naurois, M., & Rolland, L. 2009, Astropart. Phys., 32, 231
Domínguez, A., Primack, J. R., Rosario, D. J., et al. 2011, MNRAS, 410, 2556
Donath, A., Terrier, R., Remy, Q., et al. 2023, A&A, 678, A157
EHT Collaboration (Akiyama, K., et al.) 2019a, ApJ, 875, L1 (Paper I)
EHT Collaboration (Akiyama, K., et al.) 2019b, ApJ, 875, L2 (Paper II)
EHT Collaboration (Akiyama, K., et al.) 2019c, ApJ, 875, L3 (Paper III)

EHT Collaboration (Akiyama, K., et al.) 2019d, ApJ, 875, L4 (Paper IV)
EHT Collaboration (Akiyama, K., et al.) 2022, ApJ, 930, L12
EHT MWL Science Working Group, Algaba, J. C., Anczarski, J., et al. 2021, ApJ, 911, L11
EHT MWL Science Working Group, Algaba, J. C., Baloković, M., et al. 2024, A&A, 692, A140
Emery, G., Cerruti, M., Dmytriiev, A., et al. 2019, Int. Cosm. Ray Conf., 36, 668
Fitzpatrick, E. L. 1999, PASP, 111, 65
Flewelling, H. A., Magnier, E. A., Chambers, K. C., et al. 2020, ApJS, 251, 7
Fomin, V. P., Stepanian, A. A., Lamb, R. C., et al. 1994, Astropart. Phys., 2, 137
Fuentes, A., Gómez, J. L., Martí, J. M., et al. 2023, Nat. Astron., 7, 1359
Giannios, D. 2013, MNRAS, 431, 355
Goddi, C., Martí-Vidal, I., Messias, H., et al. 2021, ApJ, 910, L14
H.E.S.S. Collaboration (Abdalla, H., et al.) 2019, A&A, 627, A159
Hallum, M. K., Jorstad, S. G., Larionov, V. M., et al. 2022, ApJ, 926, 180
Hayashida, M., Madejski, G. M., Nalewajko, K., et al. 2012, ApJ, 754, 114
Hayashida, M., Nalewajko, K., Madejski, G. M., et al. 2015, ApJ, 807, 79
Hodgson, J. A., Lee, S.-S., Zhao, G.-Y., et al. 2016, J. Korean Astron. Soc., 49, 137
Hu, X.-F., Jiang, H.-X., Mizuno, Y., Fromm, C. M., & Vaidya, B. 2025, ApJ, 995, 76
Humphrey, P. J., Liu, W., & Buote, D. A. 2009, ApJ, 693, 822
Jones, T. W. 1988, ApJ, 332, 678
Jorstad, S. G., Marscher, A. P., Lister, M. L., et al. 2004, AJ, 127, 3115
Jorstad, S. G., Marscher, A. P., Larionov, V. M., et al. 2010, ApJ, 715, 362
Jorstad, S. G., Marscher, A. P., Morozova, D. A., et al. 2017, ApJ, 846, 98
Kardashev, N. S., Alakoz, A. V., Andrianov, A. S., et al. 2017, Sol. Syst. Res., 51, 535
Kawabata, K. S., Okazaki, A., Akitaya, H., et al. 1999, PASP, 111, 898
Kim, J.-Y., Krichbaum, T. P., Broderick, A. E., et al. 2020, A&A, 640, A69
Königl, A. 1980, Phys. Fluids, 23, 1083
Kostrichkin, I. M., Plavin, A. V., Pushkarev, A. B., & Butuzova, M. S. 2025, MNRAS, 537, 978
Kravchenko, E., Giroletti, M., Hada, K., et al. 2020, A&A, 637, L6
Kravchenko, E. V., Pashchenko, I. N., Homan, D. C., et al. 2025, MNRAS, 538, 2008
Kravchenko, E. V., Savolainen, T., Nikonov, A. S., et al. 2026, MNRAS, submitted
Lalakos, A., Tchekhovskoy, A., Bromberg, O., et al. 2024, ApJ, 964, 79
Lalakos, A., Tchekhovskoy, A., Most, E. R., et al. 2025, Phys. Rev. D, 112, 123044
Larionov, V. M., Jorstad, S. G., Marscher, A. P., et al. 2008, A&A, 492, 389
Larionov, V. M., Jorstad, S. G., Marscher, A. P., et al. 2020, MNRAS, 492, 3829
Lee, S.-S., Wajima, K., Algaba, J.-C., et al. 2016, ApJS, 227, 8
Li, H. Z., Xie, G. Z., Chen, L. E., et al. 2009, PASP, 121, 1172
Liodakis, I., Marscher, A. P., Agudo, I., et al. 2022, Nature, 611, 677
Liodakis, I., Kiehlmann, S., Marscher, A. P., et al. 2024, A&A, 689, A200
Lisakov, M., Jorstad, S., Wielgus, M., et al. 2025, A&A, 693, A9
Liska, M., Hesp, C., Tchekhovskoy, A., et al. 2018, MNRAS, 474, L81
Liska, M., Hesp, C., Tchekhovskoy, A., et al. 2021, MNRAS, 507, 983
Lister, M. L., Aller, M. F., Aller, H. D., et al. 2018, ApJS, 234, 12
Lister, M. L., Homan, D. C., Kellermann, K. I., et al. 2021, ApJ, 923, 30
Liu, H. T., Bai, J. M., & Ma, L. 2008, ApJ, 688, 148
Lu, R.-S., Fish, V. L., Akiyama, K., et al. 2013, ApJ, 772, 13
Madejski, G. G., & Sikora, M. 2016, ARA&A, 54, 725
MAGIC Collaboration (Albert, J., et al.) 2008, Science, 320, 1752
MAGIC Collaboration (Abe, K., et al.) 2025, A&A, 695, A217
Maraschi, L., Grandi, P., Urry, C. M., et al. 1994, ApJ, 435, L91
Marscher, A. P. 2014, ApJ, 780, 87
Marscher, A. P., & Gear, W. K. 1985, ApJ, 298, 114
Marscher, A. P., Jorstad, S. G., & Williamson, K. E. 2017, Galaxies, 5, 63
Marscher, A. P., Di Gesu, L., Jorstad, S. G., et al. 2024, Galaxies, 12, 50
Marshall, H. L., Liodakis, I., Marscher, A. P., et al. 2024, ApJ, 972, 74
Marziani, P., Sulentic, J. W., Dultzin-Hacyan, D., Calvani, M., & Moles, M. 1996, ApJS, 104, 37
Migliori, G., Siemiginowska, A., Sobolewska, M., et al. 2016, ApJ, 821, L31
Mohana, K., Gupta, A. C., Fan, J., et al. 2025, ApJ, 989, 125
Nikonov, A. S., Kovalev, Y. Y., Kravchenko, E. V., Pashchenko, I. N., & Lobanov, A. P. 2023, MNRAS, 526, 5949
Nilsson, K., Pursimo, T., Villforth, C., Lindfors, E., & Takalo, L. O. 2009, A&A, 505, 601
Pordes, R., OSG Consortium, Petravick, D., et al. 2007, J. Phys.: Conf. Ser., 78, 012057
Parsons, R. D., & Hinton, J. A. 2014, Astropart. Phys., 56, 26
Peterson, B. M. 1997, An Introduction to Active Galactic Nuclei (Cambridge University Press: Cambridge, New York)
Petropoulou, M., Giannios, D., & Sironi, L. 2016, MNRAS, 462, 3325
Prince, R. 2020, ApJ, 890, 164
Principe, G., Malyshev, D., Ballet, J., & Funk, S. 2018, A&A, 618, A22
Principe, G., Migliori, G., Johnson, T. J., et al. 2020, A&A, 635, A185
Principe, G., Di Venere, L., Orienti, M., et al. 2021, MNRAS, 507, 4564
Pushkarev, A. B., Aller, H. D., Aller, M. F., et al. 2023, MNRAS, 520, 6053
Qian, S.-J. 2011, Res. Astron. Astrophys., 11, 43
Qian, S.-J. 2012, Res. Astron. Astrophys., 12, 46
Qian, S. J., Britzen, S., Krichbaum, T. P., & Witzel, A. 2019, A&A, 621, A11
Rani, B., Krichbaum, T. P., Lee, S.-S., et al. 2017, MNRAS, 464, 418
Ressler, S. M., Combi, L., Ripperda, B., & Most, E. R. 2025, ApJ, 979, L24
Ripperda, B., Liska, M., Chatterjee, K., et al. 2022, ApJ, 924, L32
Ro, H., Kino, M., Hada, K., et al. 2026, ApJ, 999, 169
Roming, P. W. A., Kennedy, T. E., Mason, K. O., et al. 2005, Space Sci. Rev., 120, 95
Schlafly, E. F., & Finkbeiner, D. P. 2011, ApJ, 737, 103
Schmidt, G. D., Elston, R., & Lupie, O. L. 1992, AJ, 104, 1563
Sfiligoi, I., Bradley, D., Holzman, B., et al. 2009, in 2009 WRI World Congress on Computer Science and Information Engineering, CSIE 2009, 2, 428
Shepherd, M. C. 1997, ASP Conf. Ser., 125, 77
Shukla, A., & Mannheim, K. 2020, Nat. Commun., 11, 4176
Sikora, M., Stawarz, Ł., Moderski, R., Nalewajko, K., & Madejski, G. M. 2009, ApJ, 704, 38
Skrutskie, M. F., Cutri, R. M., Stiening, R., et al. 2006, AJ, 131, 1163
Smith, P. 2016, Galaxies, 4, 27
Tavecchio, F., & Ghisellini, G. 2008, MNRAS, 386, 945
Tavecchio, F., & Mazin, D. 2009, MNRAS, 392, L40
Tchekhovskoy, A., & Bromberg, O. 2016, MNRAS, 461, L46
Thekkoth, A., Sahayanathan, S., Shah, Z., Paliya, V. S., & Ravikumar, C. D. 2023, MNRAS, 526, 6364
Timmer, J., & König, M. 1995, A&A, 300, 707
Todorov, R. V., Kravchenko, E. V., Pashchenko, I. N., & Pushkarev, A. B. 2023, Astron. Rep., 67, 1275
Tokunaga, A. T., Simons, D. A., & Vacca, W. D. 2002, PASP, 114, 180
Tonry, J. L., Stubbs, C. W., Lykke, K. R., et al. 2012, ApJ, 750, 99
Toscano, T., Gómez, J. L., Zhao, G.-Y., et al. 2025, arXiv e-prints [arXiv:2509.21987]
Uttley, P., McHardy, I. M., & Vaughan, S. 2005, MNRAS, 359, 345
Vaughan, S., Edelson, R., Warwick, R. S., & Uttley, P. 2003, MNRAS, 345, 1271
Weaver, Z. R., Jorstad, S. G., Marscher, A. P., et al. 2022, ApJS, 260, 12
Wood, M., Caputo, R., Charles, E., et al. 2017, arXiv e-prints [arXiv:1707.09551]
Zhang, Y. H., Celotti, A., Treves, A., et al. 1999, ApJ, 527, 719
Zhang, H., Marscher, A. P., Guo, F., et al. 2023, ApJ, 949, 71

Authors and affiliations

G. Principe[1,2,3,⋆], J. C. Algaba[4], E. Aviano[1,2,⋆⋆], W. Y. Cheong[5,6], K. Hada[7,8], D. Haggard[9,10], A. Hahn[11], S. G. Jorstad[12], E. V. Kravchenko, Y. Kovalev[25], S. S. Lee[5], M. Lisakov[13], S. Markoff[14,15,18], A. P. Marscher[12], M. Sasada[17,7,16], P. Voitsik[25],
(The Event Horizon Telescope Collaboration),
Kazunori Akiyama[19,20,21,22], Ezequiel Albentosa-Ruíz[23], Antxon Alberdi[24], Walter Alef[25], Rohan Ganesh Amanaganti[27], Richard Anantua[28,29,30,22], Eleni Antonopoulou[31,32], Keiichi Asada[33], Rebecca Azulay[23,34,25], Anne-Kathrin Baczko[35,25], David Ball[36], Bidisha Bandyopadhyay[37], John Barrett[20], Michi Bauböck[38], Bradford A. Benson[39,40], Dan Bintley[41,42], Lindy Blackburn[22,30], Raymond Blundell[22], Katherine L. Bouman[43], Geoffrey C. Bower[41,42,44,45], Michael Bremer[46], Roger Brissenden[22], Silke Britzen[25], Avery E. Broderick[47,48,49], Dominique Broguiere[46], Thomas Bronzwaer[50], Sandra Bustamante[51], Douglas F. Carlos[52], John E. Carlstrom[53,40,54,55], Andrew Chael[56], Chi-kwan Chan[36,57,58], Chin-Shin Chang[59], Dominic O. Chang[22,30], Koushik Chatterjee[60,30,22], Erandi Chavez[22], Ming-Tang Chen[44], Yongjun Chen (陈永军)[61,62], Xiaopeng Cheng[63], Paul Chichura[54,53], Ilje Cho[64,63,24], Nicholas S. Conroy[65,22], John E. Conway[35], Thomas M. Crawford[40,53], Geoffrey B. Crew[20], Alejandro Cruz-Osorio[66], Yuzhu Cui (崔玉竹)[67], Brandon Curd[28,30,22], Rohan Dahale[24,68,69], Jordy Davelaar[70,71], Joost de Kleuver[50], Mariafelicia De Laurentis[72,73], Roger Deane[74,75,76], Jason Dexter[77], Vedant Dhruv[38], Indu K. Dihingia[78,79], Sheperd S. Doeleman[22,30], Sergio A. Dzib[25], Razieh Emami[22], Heino Falcke[50], Joseph Farah[80,81], Vincent L. Fish[20], Edward Fomalont[82], H. Alyson Ford[36], Marianna Foschi[24,43], Raquel Fraga-Encinas[50], William T. Freeman[83,84], Per Friberg[41,42], Christian M. Fromm[85,86,25], Antonio Fuentes[24], Peter Galison[30,87,88], Charles F. Gammie[38,65,89], Roberto García[46], Olivier Gentaz[46], Boris Georgiev[36], Ciriaco Goddi[52,90,91,92], Roman Gold[93,94,95], Arturo I. Gómez-Ruiz[96,97], Brissa Gomez Miller[98], José L. Gómez[24], Minfeng Gu (顾敏峰)[61,99], Mark Gurwell[22], Ronald Hesper[101], Dirk Heumann[36], Luis C. Ho (何子山)[102,103], Paul Ho[33,42,41], Mareki Honma[21,104,105], Chih-Wei L. Huang[33], Lei Huang (黄磊)[61,99], David H. Hughes[96], Shiro Ikeda[106,107,108,109], C. M. Violette Impellizzeri[110,82], Makoto Inoue[33], Sara Issaoun[22,71], Yuhei Iwata[21,104], David J. James[111,112], Buell T. Jannuzi[36], Michael Janssen[50,25], Britton Jeter[113,114], Wu Jiang (江悟)[61], Alejandra Jiménez-Rosales[50], Michael D. Johnson[22,30], Adam C. Jones[40], Abhishek V. Joshi[38], Taehyun Jung[63,115], Tomohisa Kawashima[116], Garrett K. Keating[22], Mark Kettenis[117], Dong-Jin Kim[118], Jae-Young Kim[119], Jongsoo Kim[63], Junhan Kim[120], Motoki Kino[106,121], Jakob Knollmüller[122,50], Jun Yi Koay[123,33], Prashant Kocherlakota[30,22], Yutaro Kofuji[24,21], Patrick M. Koch[33], Shoko Koyama[123,33], Carsten Kramer[46], Joana A. Kramer[124,25], Michael Kramer[25], Thomas P. Krichbaum[25], Cheng-Yu Kuo[125,33], Noemi La Bella[50], Deokhyeong Lee[64], Aviad Levis[68,126,127], Shaoliang Li[41,42], Zhiyuan Li (李志远)[128,129], Rocco Lico[130,24], Greg Lindahl[131], Michael Lindqvist[35], Jun Liu (刘俊)[25], Kuo Liu[132], Elisabetta Liuzzo[133], Wen-Ping Lo[33,134], Andrei P. Lobanov[25], Laurent Loinard[98,30], Colin J. Lonsdale[20], Amy E. Lowitz[36], Ru-Sen Lu (路如森)[61,62,25], Nicholas R. MacDonald[135,25], Jirong Mao (毛基荣)[136,137,138], Nicola Marchili[133,25], Daniel P. Marrone[36], Iván Martí-Vidal[23,34], Satoki Matsushita[33], Lynn D. Matthews[20], Lia Medeiros[27], Karl M. Menten[25,140], Hugo Messias[141,142], Izumi Mizuno[41,42], Yosuke Mizuno[79,143,86], Joshua Montgomery[100,40], Kotaro Moriyama[24,21], Monika Moscibrodzka[50], Wanga Mulaudzi[124], Cornelia Müller[25,50], Hendrik Müller[25], Alejandro Mus[90,130,144,145,146], Gibwa Musoke[124,50], Ioannis Myserlis[147], Hiroshi Nagai[106,104], Neil M. Nagar[37], Dhanya G. Nair[37,25], Masanori Nakamura[148,33], Gopal Narayanan[51], Iniyan Natarajan[149,22,30], Antonios Nathanail[31], Santiago Nvarro Fuentes[147], Joey Neilsen[150], Chunchong Ni[48,49,47], Andy Nilipour[151,152], Michael A. Nowak[153], Hiroki Okino[21,105], Héctor Raúl Olivares Sánchez[154], Feryal Özel[155], Daniel C. M. Palumbo[30,22], Georgios Filippos Paraschos[113,114,25], Jongho Park[156,157,33], Harriet Parsons[41,42], Nimesh Patel[22], Ue-Li Pen[33,47,69,127,158], Dominic W. Pesce[22,30], Vincent Piétu[46], Alexander Plavin[30,22,25], Aleksandar PopStefanija[51], Oliver Porth[124,86], Cora Prather[30], Dimitrios Psaltis[155], Hung-Yi Pu[159,160,33], Alexandra Rahlin[40], Venkatessh Ramakrishnan[161,113,114], Ramprasad Rao[22], Mark G. Rawlings[82,41,42], Angelo Ricarte[30,22], Luca Ricci[162], Bart Ripperda[69,163,127,47], Jan Röder[24], Freek Roelofs[50], Cristina Romero-Cañzales[33], Eduardo Ros[25], Arash Roshanineshat[36], Helge Rottmann[25], Alan L. Roy[25], Ignacio Ruiz[147], Chet Ruszczyk[20], Kazi L. J. Rygl[133], León D. S. Salas[124], Salvador Sánchez[147], David Sánchez-Argüelles[96,97], Miguel Sánchez-Portal[147], Ali SaraerToosi[68], Kaushik Satapathy[36],

Saurabh[25], Tuomas Savolainen[164,114,25], Karl-Friedrich Schuster[165], Zhiqiang Shen (沈志强)[61,62], Sasikumar Silpa[37], Randall Smith[22], Bong Won Sohn[63,115], Jason SooHoo[20], Kamal Souccar[51], Joshua S. Stanway[166], He Sun (孙赫)[167,168], Alexandra J. Tetarenko[169], Paul Tiede[22,30], Remo P. J. Tilanus[36], Michael Titus[20], Kenji Toma[170,171], Pablo Torne[147,25], Teresa Toscano[24,25], Efthalia Traianou[24,25], Sascha Trippe[172,173], Matthew Turk[65], Akhil Uniyal[79], Ilse van Bemmel[174], Bram van den Berg[50], Huib Jan van Langevelde[117,110], Daniel R. van Rossum[50], Sebastiano D. von Fellenberg[69,25], Jesse Vos[175], Jan Wagner[25], Zhiren Wang[47,48,49], Derek Ward-Thompson[166], John Wardle[176], Jasmin E. Washington[36], Jonathan Weintroub[22,30], Maciek Wielgus[24], Kaj Wiik[177,113,114], Michael F. Wondrak[124,139,50,178], George N. Wong[179,56], Jompoj Wongphexhauxsorn[162,25], Qingwen Wu (吴庆文)[180], Paul Yamaguchi[22], Aristomenis Yfantis[24], Doosoo Yoon[124], André Young[50], Ziri Younsi[181,86], Wei Yu (于威)[22], Feng Yuan (袁峰)[182], Ye-Fei Yuan (袁业飞)[183], Ai-Ling Zeng (曾艾玲)[24], J. Anton Zensus[25], Shuo Zhang[184], Brandon Zhao[43], Guang-Yao Zhao[25,24],

(The MAGIC collaboration),

J. Abhir[185], A. Abhishek[186], V. A. Acciari[187], A. Aguasca-Cabot[188], I. Agudo[189], I. Albanese[190], T. Aniello[191], S. Ansoldi[192,219], L. A. Antonelli[191], A. Arbet Engels[11], C. Arcaro[190], T. T. H. Arnesen[193], A. Babić[194], C. Bakshi[195], U. Barres de Almeida[196], J. A. Barrio[197], L. Barrios-Jiménez[193], I. Batković[190], J. Becerra González[193,★★★], W. Bednarek[198], E. Bernardini[190], J. Bernete[199], A. Berti[11], J. Besenrieder[11], C. Bigongiari[191], A. Biland[185], O. Blanch[187], G. Bonnoli[191], Ž. Bošnjak[194], E. Bronzini[191], I. Burelli[187], A. Campoy-Ordaz[200], A. Carosi[191], R. Carosi[201], M. Carretero-Castrillo[188], A. J. Castro-Tirado[189], D. Cerasole[202], G. Ceribella[11], A. Cerviño[197], Y. Chai[203], G. Chon[11], J. L. Contreras[197], J. Cortina[199], S. Covino[191,220], P. Da Vela[191], F. Dazzi[191], A. De Angelis[190], B. De Lotto[192], M. Delfino[187,221], J. Delgado[187,221], C. Delgado Mendez[199], F. Di Pierro[204], R. Di Tria[202], L. Di Venere[202], A. Dinesh[197], D. Dominis Prester[205], A. Donini[191], D. Dorner[206], M. Doro[190], L. Eisenberger[206], D. Elsaesser[207], L. Foffano[191], L. Font[200], F. Frías García-Lago[193], S. Fröse[207], Y. Fukazawa[208], S. Gasparyan[209], M. Gaug[200], J. G. Giesbrecht Paiva[196], N. Giglietto[202], F. Giordano[202], P. Gliwny[198], T. Gradetzke[207], R. Grau[203], J. G. Green[11], P. Günther[206], D. Hadasch[187], G. Harutyunyan[209], J. Herrera Llorente[193], D. Hrupec[210], D. Israyelyan[209], J. Jahanvi[192], I. Jiménez Martínez[11], J. Jiménez Quiles[187], S. Kankkunen[211], T. Kayanoki[208], J. Konrad[207], P. M. Kouch[211], H. Kubo[203], J. Kushida[212], M. Láinez[197], A. Lamastra[191], E. Lindfors[211], S. Lombardi[191], F. Longo[192,222], R. López-Coto[189], M. López-Moya[197], A. López-Oramas[193], S. Loporchio[202], L. Lulić[205], P. Majumdar[195], M. Makariev[213], M. Mallamaci[214], G. Maneva[213], M. Manganaro[205], S. Mangano[199], K. Mannheim[206], S. Marchesi[191], M. Mariotti[190], M. Martínez[187], P. Maruševec[194], D. Mazin[203,11], S. Menchiari[189], J. Méndez Gallego[189], S. Menon[191,223], D. Miceli[190], J. M. Miranda[186], R. Mirzoyan[11], M. Molero González[199,★★★], E. Molina[193], H. A. Mondal[203], A. Moralejo[187], C. Nanci[191], A. Negro[203], V. Neustroev[215], C. Nigro[187], L. Nikolić[186], K. Noda[203], S. Nozaki[203], A. Okumura[216], J. Otero-Santos[190], S. Paiano[191], D. Paneque[11], R. Paoletti[186], J. M. Paredes[188], M. Peresano[11], M. Persic[192,224], M. Pihet[189], G. Pirola[11], F. Podobnik[186], P. G. Prada Moroni[201], E. Prandini[190], M. Ribó[188], J. Rico[187], A. Roy[208], N. Sahakyan[209], F. G. Saturni[191], F. Schiavone[202], K. Schmitz[207], A. Sciaccaluga[191], G. Silvestri[190], A. Simongini[191], J. Sitarek[198], V. Sliusar[217], D. Sobczynska[198], A. Stamerra[191], J. Strišković[210], D. Strom[11], Y. Suda[208], M. Takahashi[216], R. Takeishi[203], J. Tartera Barberà[187], P. Temnikov[213], T. Terzić[205], M. Teshima[11,203], A. Tutone[191], S. Ubach[200], S. Ventura[186], G. Verna[186], I. Viale[204], A. Vigliano[192], C. F. Vigorito[204], E. Visentin[204], V. Vitale[218], M. Vorbrugg[206], I. Vovk[203], R. Walter[217], C. Walther[207], F. Wersig[207], P. K. H. Yeung[203],

(Other Authors),

A. Acharyya[225], F. Aharonian[226,227], H. Ashkar[228], M. Backes[229,230], M. Barnard[230], Y. Becherini[231], M. Böttcher[230], J. Bolmont[233], B. Bruno[234], T. Bylund[232], S. Casanova[235], M. Chernyakova[236,227], J. O. Chibueze[230,229], O. Chibueze[230], B. Cornejo[237], J. Damascene Mbarubucyeye[238], I. D. Davids[229], J. de Assis Scarpin[228], M. de Naurois[228], A. Dmytriiev[239], K. Egberts[240], S. Fegan[228], K. Feijen[231], M. D. Filipovic[241], G. Fontaine[228], S. Gabici[231], J. F. Glicenstein[237], P. Goswami[242], L. Heckmann[231], B. Heß[243], M. Holler[244], D. Horns[245], E. Kasai[229], K. Katarzyński[246], D. Kerszberg[233], B. Khélifi[231], K. Kosack[237], R. G. Lang[234], S. Lazarević[241], P. Liniewicz[248], A. Luashvili[230,★★★★], D. Malyshev[243], D. Malyshev[234], M. G. F. Mayer[234], M. Meyer[225], A. Mikhno[233], E. Moulin[237], H. Ndiyavala[229,230], J. Niemiec[235], P. Pichard[231], T. Preis[244], G. Pühlhofer[243], A. Quirrenbach[242], A. Reimer[244], O. Reimer[244], I. Reis[237], B. Rudak[249], K. Sabri[247], V. Sahakian[250], A. Santangelo[243], M. Sasaki[234], I. Shebalkova[236], W. Si Said[228], Ł. Stawarz[248], R. Steenkamp[229], T. Tanaka[251], G. L. Taylor[242], R. Terrier[231], Y. Tian[238],

M. Tluczykont[245], C. Venter[230], J. Vink[252], V. Voitsekhovskyi[252], S. J. Wagner[242,★★★★], A. Wierzcholska[235,242], M. Zacharias[242,230], and A. A. Zdziarski[249]

[1] Dipartimento di Fisica, Università di Trieste, I-34127 Trieste, Italy
[2] Istituto Nazionale di Fisica Nucleare, Sezione di Trieste, I-34127 Trieste, Italy
[3] INAF Istituto di Radioastronomia, Via P. Gobetti, 101, I-40129 Bologna, Italy
[4] Department of Physics, Faculty of Science, University of Malaya, 50603 Kuala Lumpur, Malaysia
[5] Korea Astronomy and Space Science Institute, 776 Daedeok-daero, Daejeon 34055, Korea
[6] University of Science and Technology, 217 Gajeong-ro, Yuseong-gu, Daejeon 34113, Korea
[7] Mizusawa VLBI Observatory, National Astronomical Observatory of Japan, 2-12 Hoshigaoka, Mizusawa, Oshu, Iwate 023-0861, Japan
[8] Graduate School of Science, Nagoya City University, Yamanohata 1, Mizuho-cho, Mizuho-ku, Nagoya 467-8501, Aichi, Japan
[9] Department of Physics, McGill University, 3600 University Street, Montreal QC H3A 2T8, Canada
[10] Trottier Space Institute at McGill, 3550 rue University, Montréal QC H3A 2A7, Canada
[11] Max-Planck-Institut für Physik, D-85748 Garching, Germany
[12] Institute for Astrophysical Research, Boston University, 725 Commonwealth Ave., Boston 02215, MA, USA
[13] Instituto de Física, Pontificia Universidad Católica de Valparaíso, Casilla 4059, Valparaíso, Chile
[14] API–Anton Pannekoek Institute for Astronomy, University of Amsterdam, Science Park 904, 1098 XH Amsterdam, The Netherlands
[15] GRAPPA–Gravitation and AstroParticle Physics Amsterdam, University of Amsterdam, 1098 XH Amsterdam, The Netherlands
[16] Hiroshima Astrophysical Science Center, Hiroshima University, 1-3-1 Kagamiyama, Higashi-Hiroshima, Hiroshima 739-8526, Japan
[17] Department of Physics, Tokyo Institute of Technology, 2-12-1 Ookayama, Meguro-ku, Tokyo 152-8551, Japan
[18] Institute of Astronomy, University of Cambridge, Madingley Road, Cambridge CB3 0HA, United Kingdom
[19] Institute of Sensors, Signals and Systems, Heriot-Watt University, Edinburgh EH14 4AS, United Kingdom
[20] Massachusetts Institute of Technology Haystack Observatory, 99 Millstone Road, Westford, MA 01886, USA
[21] Mizusawa VLBI Observatory, National Astronomical Observatory of Japan, 2-12 Hoshigaoka, Mizusawa, Oshu, Iwate 023-0861, Japan
[22] Center for Astrophysics | Harvard and Smithsonian, 60 Garden Street, Cambridge, MA 02138, USA
[23] Departament d'Astronomia i Astrofísica, Universitat de València, C. Dr. Moliner 50, E-46100 Burjassot, València, Spain
[24] Instituto de Astrofísica de Andalucía-CSIC, Glorieta de la Astronomía s/n, E-18008 Granada, Spain
[25] Max-Planck-Institut für Radioastronomie, Auf dem Hügel 69, D-53121 Bonn, Germany
[26] Centre for Astronomy and Astrophysics Research, Department of Physics, Faculty of Science, Universiti Malaya, 50603 Kuala Lumpur, Malaysia
[27] Center for Gravitation, Cosmology and Astrophysics, Department of Physics, University of Wisconsin–Milwaukee, Milwaukee, WI 53201, USA
[28] Department of Physics and Astronomy, The University of Texas at San Antonio, One UTSA Circle, San Antonio, TX 78249, USA
[29] Physics and Astronomy Department, Rice University, Houston, TX 77005-1827, USA
[30] Black Hole Initiative at Harvard University, 20 Garden Street, Cambridge, MA 02138, USA
[31] Research Center for Astronomy, Academy of Athens, Soranou Efessiou 4, 115 27 Athens, Greece
[32] Department of Physics, National and Kapodistrian University of Athens, Panepistimiopolis GR 15783, Zografos, Greece
[33] Institute of Astronomy and Astrophysics, Academia Sinica, 11F of Astronomy-Mathematics Building, AS/NTU No. 1, Sec. 4, Roosevelt Rd., Taipei 106216, Taiwan, ROC
[34] Observatori Astronòmic, Universitat de València, C. Catedrático José Beltrán 2, E-46980 Paterna, València, Spain
[35] Department of Physics and Astronomy, Chalmers University of Technology, Onsala Space Observatory, SE-439 92 Onsala, Sweden
[36] Steward Observatory and Department of Astronomy, University of Arizona, 933 N. Cherry Ave., Tucson, AZ 85721, USA
[37] Astronomy Department, Universidad de Concepción, Casilla 160-C, Concepción, Chile
[38] Department of Physics, University of Illinois, 1110 West Green Street, Urbana, IL 61801, USA
[39] Fermi National Accelerator Laboratory, MS209, P.O. Box 500, Batavia, IL 60510, USA
[40] Department of Astronomy and Astrophysics, University of Chicago, 5640 South Ellis Avenue, Chicago, IL 60637, USA
[41] East Asian Observatory, 660 N. A'ohoku Place, Hilo, HI 96720, USA
[42] James Clerk Maxwell Telescope (JCMT), 660 N. A'ohoku Place, Hilo, HI 96720, USA
[43] California Institute of Technology, 1200 East California Boulevard, Pasadena, CA 91125, USA
[44] Institute of Astronomy and Astrophysics, Academia Sinica, 645 N. A'ohoku Place, Hilo, HI 96720, USA
[45] Department of Physics and Astronomy, University of Hawaii at Manoa, 2505 Correa Road, Honolulu, HI 96822, USA
[46] Institut de Radioastronomie Millimétrique (IRAM), 300 rue de la Piscine, F-38400 Saint-Martin-d'Hères, France
[47] Perimeter Institute for Theoretical Physics, 31 Caroline Street North, Waterloo ON N2L 2Y5, Canada
[48] Department of Physics and Astronomy, University of Waterloo, 200 University Avenue West, Waterloo ON N2L 3G1, Canada
[49] Waterloo Centre for Astrophysics, University of Waterloo, Waterloo ON N2L 3G1, Canada
[50] Department of Astrophysics, Institute for Mathematics, Astrophysics and Particle Physics (IMAPP), Radboud University, P.O. Box 9010, 6500 GL Nijmegen, The Netherlands
[51] Department of Astronomy, University of Massachusetts, Amherst, MA 01003, USA
[52] Instituto de Astronomia, Geofísica e Ciências Atmosféricas, Universidade de São Paulo, R. do Matão, 1226, São Paulo SP 05508-090, Brazil
[53] Kavli Institute for Cosmological Physics, University of Chicago, 5640 South Ellis Avenue, Chicago, IL 60637, USA
[54] Department of Physics, University of Chicago, 5720 South Ellis Avenue, Chicago, IL 60637, USA
[55] Enrico Fermi Institute, University of Chicago, 5640 South Ellis Avenue, Chicago, IL 60637, USA
[56] Princeton Gravity Initiative, Jadwin Hall, Princeton University, Princeton, NJ 08544, USA
[57] Data Science Institute, University of Arizona, 1230 N. Cherry Ave., Tucson, AZ 85721, USA
[58] Program in Applied Mathematics, University of Arizona, 617 N. Santa Rita, Tucson, AZ 85721, USA
[59] Department of Astronomy, University of Geneva, Chemin Pegasi 51, 1290 Versoix, Switzerland
[60] Department of Physics, University of Maryland, 7901 Regents Drive, College Park, MD 20742, USA
[61] Shanghai Astronomical Observatory, Chinese Academy of Sciences, 80 Nandan Road, Shanghai 200030, PR China
[62] Key Laboratory of Radio Astronomy and Technology, Chinese Academy of Sciences, Chaoyang District, Beijing 100101, PR China

[63] Korea Astronomy and Space Science Institute, Daedeok-daero 776, Yuseong-gu, Daejeon 34055, Republic of Korea
[64] Department of Astronomy, Kyungpook National University, 80 Daehak-ro, Buk-gu, Daegu 41566, Republic of Korea
[65] Department of Astronomy, University of Illinois at Urbana-Champaign, 1002 West Green Street, Urbana, IL 61801, USA
[66] Instituto de Astronomía, Universidad Nacional Autónoma de México (UNAM), Apdo Postal 70-264, Ciudad de México, Mexico
[67] Institute of Astrophysics, Central China Normal University, Wuhan 430079, PR China
[68] Department of Computer Science, University of Toronto, 40 St. George St., Toronto, ON M5S 2E4, Canada
[69] Canadian Institute for Theoretical Astrophysics, University of Toronto, 60 St. George Street, Toronto ON M5S 3H8, Canada
[70] Department of Astrophysical Sciences, Peyton Hall, Princeton University, Princeton, NJ 08544, USA
[71] NASA Hubble Fellowship Program, Einstein Fellow
[72] Dipartimento di Fisica "E. Pancini", Universitá di Napoli "Federico II", Compl. Univ. di Monte S. Angelo, I-80126 Napoli, Italy
[73] INFN Sez. di Napoli, Compl. Univ. di Monte S. Angelo, Edificio G, Via Cinthia, I-80126 Napoli, Italy
[74] Wits Centre for Astrophysics, University of the Witwatersrand, 1 Jan Smuts Avenue, Braamfontein, Johannesburg 2050, South Africa
[75] Department of Physics, University of Pretoria, Hatfield, Pretoria 0028, South Africa
[76] Centre for Radio Astronomy Techniques and Technologies, Department of Physics and Electronics, Rhodes University, Makhanda 6140, South Africa
[77] JILA and Department of Astrophysical and Planetary Sciences, University of Colorado, Boulder, CO 80309, USA
[78] Institute of Fundamental Physics and Quantum Technology, and School of Physical Science and Technology, Ningbo University, Ningbo, Zhejiang 315211, PR China
[79] Tsung-Dao Lee Institute, Shanghai Jiao Tong University, Shengrong Road 520, Shanghai 201210, PR China
[80] Las Cumbres Observatory, 6740 Cortona Drive, Suite 102, Goleta, CA 93117-5575, USA
[81] Department of Physics, University of California, Santa Barbara, CA 93106-9530, USA
[82] National Radio Astronomy Observatory, 520 Edgemont Road, Charlottesville, VA 22903, USA
[83] Department of Electrical Engineering and Computer Science, Massachusetts Institute of Technology, Cambridge, MA 02142, USA
[84] Google Research, 355 Main St., Cambridge, MA 02142, USA
[85] Institut für Theoretische Physik und Astrophysik, Universität Würzburg, Emil-Fischer-Str. 31, D-97074 Würzburg, Germany
[86] Institut für Theoretische Physik, Goethe-Universität Frankfurt, Max-von-Laue-Straße 1, D-60438 Frankfurt am Main, Germany
[87] Department of History of Science, Harvard University, Cambridge, MA 02138, USA
[88] Department of Physics, Harvard University, Cambridge, MA 02138, USA
[89] NCSA, University of Illinois, 1205 W. Clark St., Urbana, IL 61801, USA
[90] Dipartimento di Fisica, Universitá degli Studi di Cagliari, SP Monserrato-Sestu km 0.7, I-09042 Monserrato (CA), Italy
[91] INAF – Osservatorio Astronomico di Cagliari, via della Scienza 5, I-09047 Selargius (CA), Italy
[92] INFN, sezione di Cagliari, I-09042 Monserrato (CA), Italy
[93] Institute for Mathematics and Interdisciplinary Center for Scientific Computing, Heidelberg University, Heidelberg 69120, Germany
[94] Institut für Theoretische Physik, Universität Heidelberg, Philosophenweg 16, 69120 Heidelberg, Germany
[95] CP3-Origins, University of Southern Denmark, Campusvej 55, DK-5230 Odense, Denmark
[96] Instituto Nacional de Astrofísica, Óptica y Electrónica, Apartado Postal 51 y 216, 72000 Puebla Pue, México
[97] Consejo Nacional de Humanidades, Ciencia y Tecnología, Av. Insurgentes Sur 1582, 03940 Ciudad de México, México
[98] Instituto de Radioastronomía y Astrofísica, Universidad Nacional Autónoma de México, Morelia 58089, México
[99] Key Laboratory for Research in Galaxies and Cosmology, Chinese Academy of Sciences, Shanghai 200030, PR China
[100] Trottier Space Institute at McGill, 3550 rue University, Montréal QC H3A 2A7, Canada
[101] NOVA Sub-mm Instrumentation Group, Kapteyn Astronomical Institute, University of Groningen, 9747 AD Groningen, The Netherlands
[102] Department of Astronomy, School of Physics, Peking University, Beijing 100871, PR China
[103] Kavli Institute for Astronomy and Astrophysics, Peking University, Beijing 100871, PR China
[104] Department of Astronomical Science, The Graduate University for Advanced Studies (SOKENDAI), Mitaka, Tokyo 181-8588, Japan
[105] Department of Astronomy, Graduate School of Science, The University of Tokyo, 7-3-1 Hongo, Bunkyo-ku, Tokyo 113-0033, Japan
[106] National Astronomical Observatory of Japan, 2-21-1 Osawa, Mitaka, Tokyo 181-8588, Japan
[107] The Institute of Statistical Mathematics, 10-3 Midori-cho, Tachikawa, Tokyo 190-8562, Japan
[108] Department of Statistical Science, The Graduate University for Advanced Studies (SOKENDAI), Tokyo 190-8562, Japan
[109] Kavli Institute for the Physics and Mathematics of the Universe, The University of Tokyo, 5-1-5 Kashiwanoha, Kashiwa 277-8583, Japan
[110] Leiden Observatory, Leiden University, Postbus 2300, 9513 RA Leiden, The Netherlands
[111] ASTRAVEO LLC, PO Box 1668, Gloucester, MA 01931, USA
[112] Applied Materials Inc., 35 Dory Road, Gloucester, MA 01930, USA
[113] Finnish Centre for Astronomy with ESO, University of Turku, FI-20014 Turun Yliopisto, Finland
[114] Aalto University Metsähovi Radio Observatory, Metsähovintie 114, FI-02540 Kylmälä, Finland
[115] Korea National University of Science and Technology, Gajeong-ro 217, Yuseong-gu, Daejeon 34113, Republic of Korea
[116] National Institute of Technology, Ichinoseki College, Takanashi, Hagisho, Ichinoseki, Iwate 021-8511, Japan
[117] Joint Institute for VLBI ERIC (JIVE), Oude Hoogeveensedijk 4, 7991 PD Dwingeloo, The Netherlands
[118] CSIRO, Space and Astronomy, PO Box 76, Epping NSW 1710, Australia
[119] Department of Physics, Ulsan National Institute of Science and Technology (UNIST), Ulsan 44919, Republic of Korea
[120] Department of Physics, Korea Advanced Institute of Science and Technology (KAIST), Daejeon 34141, Republic of Korea
[121] Kogakuin University of Technology and Engineering, Academic Support Center, 2665-1 Nakano, Hachioji, Tokyo 192-0015, Japan
[122] Max-Planck-Institut für Astrophysik, Karl-Schwarzschild-Str. 1, 85748 Garching, Germany
[123] Graduate School of Science and Technology, Niigata University, 8050 Ikarashi 2-no-cho, Nishi-ku, Niigata 950-2181, Japan
[124] Anton Pannekoek Institute for Astronomy, University of Amsterdam, Science Park 904, 1098 XH Amsterdam, The Netherlands
[125] Physics Department, National Sun Yat-Sen University, No. 70, Lien-Hai Road, Kaosiung City 80424, Taiwan, ROC
[126] David A. Dunlap Department of Astronomy and Astrophysics, University of Toronto, 50 St. George St, M5S 3H4 ON, Canada
[127] Dunlap Institute for Astronomy and Astrophysics, University of Toronto, 50 St. George Street, Toronto ON M5S 3H4, Canada
[128] School of Astronomy and Space Science, Nanjing University, Nanjing 210023, PR China
[129] Key Laboratory of Modern Astronomy and Astrophysics, Nanjing University, Nanjing 210023, PR China
[130] INAF-Istituto di Radioastronomia, Via P. Gobetti 101, I-40129 Bologna, Italy

[131] Common Crawl Foundation, 9663 Santa Monica Blvd. 425, Beverly Hills, CA 90210, USA
[132] Key Laboratory of Radio Astronomy and Technology, Shanghai Astronomical Observatory, CAS, Shanghai 200030, PR China
[133] INAF-Istituto di Radioastronomia and Italian ALMA Regional Centre, Via P. Gobetti 101, I-40129 Bologna, Italy
[134] Department of Physics, National Taiwan University, No. 1, Sec. 4, Roosevelt Rd., Taipei 106216, Taiwan, ROC
[135] Department of Physics and Astronomy, University of Mississippi, Mississippi 38677, USA
[136] Yunnan Observatories, Chinese Academy of Sciences, 650011 Kunming, Yunnan Province, PR China
[137] Center for Astronomical Mega-Science, Chinese Academy of Sciences, Chaoyang District, Beijing 100012, PR China
[138] Key Laboratory for the Structure and Evolution of Celestial Objects, Chinese Academy of Sciences, 650011 Kunming, PR China
[139] Gravitation and Astroparticle Physics Amsterdam (GRAPPA) Institute, University of Amsterdam, Science Park 904, 1098 XH Amsterdam, The Netherlands
[140] Deceased
[141] Joint ALMA Observatory, Alonso de Córdova 3107, Vitacura, 763-0355 Santiago, Chile
[142] European Southern Observatory, Alonso de Córdova 3107, Vitacura, Casilla 19001, Santiago, Chile
[143] School of Physics and Astronomy, Shanghai Jiao Tong University, 800 Dongchuan Road, Shanghai 200240, PR China
[144] Soft Computing, Image Processing and Aggregation Research Group (SCOPIA) and Modelling and Imaging Radio Astronomical Data (MIRADA), Dept. of Mathematics and Computer Science, University of the Balearic Islands, Palma 07122, Spain
[145] Artificial Intelligence Research Institute of the Balearic Islands (IAIB), Palma 07122, Spain
[146] Health Research Institute of the Balearic Islands (IdISBa), 07010 Palma de Mallorca, Spain
[147] Institut de Radioastronomie Millimétrique (IRAM), Avenida Divina Pastora 7, Local 20, E-18012 Granada, Spain
[148] National Institute of Technology, Hachinohe College, 16-1 Uwanotai, Tamonoki, Hachinohe City, Aomori 039-1192, Japan
[149] SKA Observatory, Jodrell Bank, Lower Withington, Macclesfield SK11 9FT, UK
[150] Department of Physics, Villanova University, 800 Lancaster Avenue, Villanova, PA 19085, USA
[151] Cavendish Astrophysics, University of Cambridge, Madingley Road, Cambridge CB3 0HA, UK
[152] Kavli Institute for Cosmology, University of Cambridge, Madingley Road, Cambridge CB3 0HA, UK
[153] Physics Department, Washington University, CB 1105, St. Louis, MO 63130, USA
[154] Departamento de Matemática da Universidade de Aveiro and Centre for Research and Development in Mathematics and Applications (CIDMA), Campus de Santiago, 3810-193 Aveiro, Portugal
[155] School of Physics, Georgia Institute of Technology, 837 State St NW, Atlanta, GA 30332, USA
[156] School of Space Research, Kyung Hee University, 1732, Deogyeong-daero, Giheung-gu, Yongin-si, Gyeonggi-do 17104, Republic of Korea
[157] G-LAMP NEXUS Institute, Kyung Hee University, Yongin 17104, Republic of Korea
[158] Canadian Institute for Advanced Research, 180 Dundas St West, Toronto ON M5G 1Z8, Canada
[159] Department of Physics, National Taiwan Normal University, No. 88, Sec. 4, Tingzhou Rd., Taipei 116, Taiwan, ROC
[160] Center of Astronomy and Gravitation, National Taiwan Normal University, No. 88, Sec. 4, Tingzhou Road, Taipei 116, Taiwan, ROC
[161] Signal Processing Research Centre, Tampere University, FI-33720 Tampere, Finland
[162] Julius-Maximilians-Universität Würzburg, Fakultät für Physik und Astronomie, Institut für Theoretische Physik und Astrophysik, Lehrstuhl für Astronomie, Emil-Fischer-Str. 31, D-97074 Würzburg, Germany
[163] Department of Physics, University of Toronto, 60 St. George Street, Toronto ON M5S 1A7, Canada
[164] Aalto University Department of Electronics and Nanoengineering, PL 15500, FI-00076 Aalto, Finland
[165] Institut de Radioastronomie Millimétrique (IRAM), 300 rue de la Piscine, F-38406 Saint Martin d'Hères, France
[166] Jeremiah Horrocks Institute, University of Lancashire, Preston PR1 2HE, UK
[167] National Biomedical Imaging Center, Peking University, Beijing 100871, PR China
[168] College of Future Technology, Peking University, Beijing 100871, PR China
[169] Department of Physics and Astronomy, University of Lethbridge, Lethbridge, Alberta T1K 3M4, Canada
[170] Frontier Research Institute for Interdisciplinary Sciences, Tohoku University, Sendai 980-8578, Japan
[171] Astronomical Institute, Tohoku University, Sendai 980-8578, Japan
[172] Department of Physics and Astronomy, Seoul National University, Gwanak-gu, Seoul 08826, Republic of Korea
[173] SNU Astronomy Research Center, Seoul National University, Gwanak-gu, Seoul 08826, Republic of Korea
[174] ASTRON, Oude Hoogeveensedijk 4, 7991 PD Dwingeloo, The Netherlands
[175] Centre for Mathematical Plasma Astrophysics, Department of Mathematics, KU Leuven, Celestijnenlaan 200B, B-3001 Leuven, Belgium
[176] Physics Department, Brandeis University, 415 South Street, Waltham, MA 02453, USA
[177] Tuorla Observatory, Department of Physics and Astronomy, University of Turku, FI-20014 Turun Yliopisto, Finland
[178] Excellence Fellow at Radboud University, Nijmegen, The Netherlands
[179] School of Natural Sciences, Institute for Advanced Study, 1 Einstein Drive, Princeton, NJ 08540, USA
[180] School of Physics, Huazhong University of Science and Technology, Wuhan, Hubei 430074, PR China
[181] Mullard Space Science Laboratory, University College London, Holmbury St. Mary, Dorking, Surrey RH5 6NT, UK
[182] Center for Astronomy and Astrophysics and Department of Physics, Fudan University, Shanghai 200438, PR China
[183] Astronomy Department, University of Science and Technology of China, Hefei 230026, PR China
[184] Department of Physics and Astronomy, Michigan State University, 567 Wilson Rd, East Lansing, MI 48824, USA
[185] ETH Zürich, CH-8093 Zürich, Switzerland
[186] Università di Siena and INFN Pisa, I-53100 Siena, Italy
[187] Institut de Física d'Altes Energies (IFAE), The Barcelona Institute of Science and Technology (BIST), E-08193 Bellaterra (Barcelona), Spain
[188] Universitat de Barcelona, ICCUB, IEEC-UB, E-08028 Barcelona, Spain
[189] Instituto de Astrofísica de Andalucía-CSIC, Glorieta de la Astronomía s/n, 18008 Granada, Spain
[190] Università di Padova and INFN, I-35131 Padova, Italy
[191] National Institute for Astrophysics (INAF), I-00136 Rome, Italy
[192] Università di Udine and INFN Trieste, I-33100 Udine, Italy
[193] Instituto de Astrofísica de Canarias and Dpto. de Astrofísica, Universidad de La Laguna, E-38200 La Laguna, Tenerife, Spain
[194] Croatian MAGIC Group: University of Zagreb, Faculty of Electrical Engineering and Computing (FER), 10000 Zagreb, Croatia
[195] Saha Institute of Nuclear Physics, A CI of Homi Bhabha National Institute, Kolkata 700064, West Bengal, India
[196] Centro Brasileiro de Pesquisas Físicas (CBPF), 22290-180 URCA Rio de Janeiro (RJ), Brazil

[197] IPARCOS Institute and EMFTEL Department, Universidad Complutense de Madrid, E-28040 Madrid, Spain
[198] University of Lodz, Faculty of Physics and Applied Informatics, Department of Astrophysics, 90-236 Lodz, Poland
[199] Centro de Investigaciones Energéticas, Medioambientales y Tecnológicas, E-28040 Madrid, Spain
[200] Departament de Física, and CERES-IEEC, Universitat Autònoma de Barcelona, E-08193 Bellaterra, Spain
[201] Università di Pisa and INFN Pisa, I-56126 Pisa, Italy
[202] INFN MAGIC Group: INFN Sezione di Bari and Dipartimento Interateneo di Fisica dell'Università e del Politecnico di Bari, I-70125 Bari, Italy
[203] Japanese MAGIC Group: Institute for Cosmic Ray Research (ICRR), The University of Tokyo, Kashiwa 277-8582, Chiba, Japan
[204] INFN MAGIC Group: INFN Sezione di Torino and Università degli Studi di Torino, I-10125 Torino, Italy
[205] Croatian MAGIC Group: University of Rijeka, Faculty of Physics, 51000 Rijeka, Croatia
[206] Universität Würzburg, D-97074 Würzburg, Germany
[207] Technische Universität Dortmund, D-44221 Dortmund, Germany
[208] Japanese MAGIC Group: Physics Program, Graduate School of Advanced Science and Engineering, Hiroshima University, 739-8526 Hiroshima, Japan
[209] Armenian MAGIC Group: ICRANet-Armenia, 0019 Yerevan, Armenia
[210] Croatian MAGIC Group: Josip Juraj Strossmayer University of Osijek, Department of Physics, 31000 Osijek, Croatia
[211] Finnish MAGIC Group: Finnish Centre for Astronomy with ESO, Department of Physics and Astronomy, University of Turku, FI-20014 Turku, Finland
[212] Japanese MAGIC Group: Department of Physics, Tokai University, Hiratsuka 259-1292, Kanagawa, Japan
[213] Inst. for Nucl. Research and Nucl. Energy, Bulgarian Academy of Sciences, BG-1784 Sofia, Bulgaria
[214] INFN MAGIC Group: INFN Sezione di Catania and Dipartimento di Fisica e Astronomia, University of Catania, I-95123 Catania, Italy
[215] Finnish MAGIC Group: Space Physics and Astronomy Research Unit, University of Oulu, FI-90014 Oulu, Finland
[216] Japanese MAGIC Group: Institute for Space-Earth Environmental Research and Kobayashi-Maskawa Institute for the Origin of Particles and the Universe, Nagoya University, 464-6801 Nagoya, Japan
[217] University of Geneva, Chemin d'Ecogia 16, CH-1290 Versoix, Switzerland
[218] INFN MAGIC Group: INFN Roma Tor Vergata, I-00133 Roma, Italy
[219] also at International Center for Relativistic Astrophysics (ICRA), Rome, Italy
[220] also at Como Lake centre for AstroPhysics (CLAP), DiSAT, Università dell'Insubria, via Valleggio 11, 22100 Como, Italy
[221] also at Port d'Informació Científica (PIC), E-08193 Bellaterra (Barcelona), Spain
[222] also at Dipartimento di Fisica, Università di Trieste, I-34127 Trieste, Italy
[223] Dipartimento di Fisica, Università di Roma Tor Vergata, Via della Ricerca Scientifica, 1, Roma I-00133, Italy
[224] also at INAF Padova
[225] University of Southern Denmark, Odense, Denmark
[226] Yerevan State University, 1 Alek Manukyan St, Yerevan 0025, Armenia
[227] Astronomy and Astrophysics Section, School of Cosmic Physics, Dublin Institute for Advanced Studies, DIAS Dunsink Observatory, Dublin D15 XR2R, Ireland
[228] Laboratoire Leprince-Ringuet, École Polytechnique, CNRS, Institut Polytechnique de Paris, F-91128 Palaiseau, France
[229] University of Namibia, Department of Physics, Private Bag 13301, Windhoek 10005, Namibia
[230] Centre for Space Research, North-West University, Potchefstroom 2520, South Africa
[231] Université Paris Cité, CNRS, Astroparticule et Cosmologie, F-75013 Paris, France
[232] LUX, Observatoire de Paris, Université PSL, CNRS, Sorbonne Université, 5 Pl. Jules Janssen, 92190 Meudon, France
[233] Sorbonne Université, CNRS/IN2P3, Laboratoire de Physique Nucléaire, et de Hautes Energies, LPNHE, 4 place Jussieu, 75005 Paris, France
[234] Friedrich-Alexander-Universität Erlangen-Nürnberg, Erlangen Centre for Astroparticle Physics, 91058 Erlangen, Germany
[235] Instytut Fizyki Jadrowej PAN, ul. Radzikowskiego 152, ul. Radzikowskiego 152, 31-342 Kraków, Poland
[236] School of Physical Sciences and Centre for Astrophysics and Relativity, Dublin City University, Glasnevin, Dublin D09 W6Y4, Ireland
[237] IRFU, CEA, Université Paris-Saclay, F-91191 Gif-sur-Yvette, France
[238] Deutsches Elektronen-Synchrotron DESY, Platanenallee 6, 15738 Zeuthen, Germany
[239] School of Physics, University of the Witwatersrand, 1 Jan Smuts Avenue, Braamfontein, Johannesburg 2050, South Africa
[240] Institut für Physik und Astronomie, Universität Potsdam, Karl-Liebknecht-Strasse 24/25, D 14476 Potsdam, Germany
[241] School of Science, Western Sydney University, Locked Bag 1797, Penrith South DC NSW 2751, Australia
[242] Landessternwarte, Universität Heidelberg, Königstuhl, D 69117 Heidelberg, Germany
[243] Institut für Astronomie und Astrophysik, Universität Tübingen, Sand 1, D 72076 Tübingen, Germany
[244] Universität Innsbruck, Institut für Astro- und Teilchenphysik, Technikerstraße 25, 6020 Innsbruck, Austria
[245] Universität Hamburg, Institut für Experimentalphysik, Luruper Chaussee 149, D 22761 Hamburg, Germany
[246] Institute of Astronomy, Faculty of Physics, Astronomy and Informatics, Nicolaus Copernicus University, 87-100 Torun, Poland
[247] Laboratoire Univers et Particules de Montpellier, Université Montpellier, CNRS/IN2P3, CC 72, F-34095 Montpellier Cedex 5, France
[248] Obserwatorium Astronomiczne, Uniwersytet Jagielloński, ul. Orla 171, 30-244 Kraków, Poland
[249] Nicolaus Copernicus Astronomical Center, Polish Academy of Sciences, ul. Bartycka 18, 00-716 Warsaw, Poland
[250] Yerevan Physics Institute, 2 Alikhanian Brothers St., 0036 Yerevan, Armenia
[251] Department of Physics, Konan University, 8-9-1 Okamoto, Higashinada, Kobe, Hyogo 658-8501, Japan
[252] GRAPPA, Anton Pannekoek Institute for Astronomy, University of Amsterdam, Science Park 904, 1098 XH Amsterdam, The Netherlands
[253] Independent researcher

⋆ First author and project coordinator:
giacomo.principe@inaf.it
⋆⋆ *Fermi*-LAT corresponding author;
ermes.aviano@phd.units.it
⋆⋆⋆ MAGIC corresponding authors; contact.magic@mpp.mpg.de
⋆⋆⋆⋆ For questions concerning H.E.S.S. results.

Appendix A: Acknowledgements

Acknowledgements. G.P acknowledges the CINECA award under the ISCRA initiative, for the availability of high performance computing resources and support. G.P. acknowledge also partial support by ICSC – Centro Nazionale di Ricerca in High Performance Computing, Big Data and Quantum Computing, funded by European Union – NextGenerationEU.

The Event Horizon Telescope Collaboration thanks the following organizations and programs: the Academia Sinica; the Research Council of Finland (project 362572); the Agencia Nacional de Investigación y Desarrollo (ANID), Chile via NCN19_058 (TITANs), Fondecyt 1221421 and BASAL FB210003; the Alexander von Humboldt Stiftung (including the Feodor Lynen Fellowship); an Alfred P. Sloan Research Fellowship; Allegro, the European ALMA Regional Centre node in the Netherlands, the NL astronomy research network NOVA and the astronomy institutes of the University of Amsterdam, Leiden University, and Radboud University; the ALMA North America Development Fund; the Astrophysics and High Energy Physics programme by MCIN (with funding from European Union NextGenerationEU, PRTR-C17I1); the Black Hole Initiative, which is funded by grants from the John Templeton Foundation (60477, 61497, 62286) and the Gordon and Betty Moore Foundation (Grants GBMF-8273, GBMF12987) – although the opinions expressed in this work are those of the authors and do not necessarily reflect the views of these Foundations; the Black Hole Initiative, which is funded by grants from the John Templeton Foundation and the Gordon and Betty Moore Foundation (although the opinions expressed in this work are those of the author(s) and do not necessarily reflect the views of these Foundations); the Brinson Foundation; the Canada Research Chairs (CRC) program; Chandra DD7-18089X and TM6-17006X; the China Scholarship Council; the China Postdoctoral Science Foundation fellowships (2020M671266, 2022M712084); ANID through Fondecyt Postdoctorado (project 3250762); Conicyt through Fondecyt Postdoctorado (project 3220195); Consejo Nacional de Humanidades, Ciencia y Tecnología (CONAHCYT, Mexico, projects U0004-246083, U0004-259839, F0003-272050, M0037-279006, F0003-281692, 104497, 275201, 263356, CBF2023-2024-1102, 257435); the Colfuturo Scholarship; the Consejo Superior de Investigaciones ientíficas (grant 2019AEP112); the Delaney Family via the Delaney Family John A. Wheeler Chair at Perimeter Institute; Dirección General de Asuntos del Personal Académico-Universidad Nacional Autónoma de México (DGAPA-UNAM, projects IN112820 and IN108324); the Dutch Research Council (NWO) for the VICI award (grant 639.043.513), the grant OCENW.KLEIN.113, and the Dutch Black Hole Consortium (with project No. NWA 1292.19.202) of the research programme the National Science Agenda; the Dutch National Supercomputers, Cartesius and Snellius (NWO grant 2021.013); the EACOA Fellowship awarded by the East Asia Core Observatories Association, which consists of the Academia Sinica Institute of Astronomy and Astrophysics, the National Astronomical Observatory of Japan, Center for Astronomical Mega-Science, Chinese Academy of Sciences, and the Korea Astronomy and Space Science Institute; the European Research Council (ERC) Synergy Grant "BlackHoleCam: Imaging the Event Horizon of Black Holes" (grant 610058) and Synergy Grant "BlackHolistic: Colour Movies of Black Holes: Understanding Black Hole Astrophysics from the Event Horizon to Galactic Scales" (grant 10107164); the European Union Horizon 2020 research and innovation programme under grant agreements BlackHolistic (No. 101071643), RadioNet (No. 730562), M2FINDERS (No. 101018682); the European Research Council for advanced grant "JETSET: Launching, propagation and emission of relativistic jets from binary mergers and across mass scales" (grant No. 884631); the European Horizon Europe staff exchange (SE) programme HORIZON-MSCA-2021-SE-01 grant NewFunFiCO (No. 10108625); the Horizon ERC Grants 2021 programme under grant agreement No. 101040021; the FAPESP (Fundação de Amparo á Pesquisa do Estado de São Paulo) under grant 2021/01183-8; the Fondes de Recherche Nature et Technologies (FRQNT); the Fondo CAS-ANID folio CAS220010; the Generalitat Valenciana (grants APOSTD/2018/177 and ASFAE/2022/018) and GenT Program (project CIDEGENT/2018/021); the Gordon and Betty Moore Foundation (GBMF-3561, GBMF-5278, GBMF-10423); the Institute for Advanced Study; the ICSC – Centro Nazionale di Ricerca in High Performance Computing, Big Data and Quantum Computing, funded by European Union – NextGenerationEU; the Istituto Nazionale di Fisica Nucleare (INFN) sezione di Napoli, iniziative specifiche TEONGRAV; the International Max Planck Research School for Astronomy and Astrophysics at the Universities of Bonn and Cologne; the Italian Ministry of University and Research (MUR)– Project CUP F53D23001260001, funded by the European Union – NextGenerationEU; Deutsche Forschungsgemeinschaft (DFG) research grant "Jet physics on horizon scales and beyond" (grant No. 443220636) and DFG research grant 443220636; Joint Columbia/Flatiron Postdoctoral Fellowship (research at the Flatiron Institute is supported by the Simons Foundation); the Japan Ministry of Education, Culture, Sports, Science and Technology (MEXT; grant JPMXP1020200109); the Japan Society for the Promotion of Science (JSPS) Grant-in-Aid for JSPS Research Fellowship (JP17J08829); the Joint Institute for Computational Fundamental Science, Japan; the Key Research Program of Frontier Sciences, Chinese Academy of Sciences (CAS, grants QYZDJ-SSW-SLH057, QYZDJSSW-SYS008, ZDBS-LY-SLH011); the Leverhulme Trust Early Career Research Fellowship; the Max-Planck-Gesellschaft (MPG); the Max Planck Partner Group of the MPG and the CAS; the MEXT/JSPS KAKENHI (grants 18KK0090, JP21H01137, JP18H03721, JP18K13594, 18K03709, JP19K14761, 18H01245, 25120007, 19H01943, 21H01137, 21H04488, 22H00157, 23K03453); the MICINN Research Projects PID2019-108995GB-C22, PID2022-140888NB-C22; the MIT International Science and Technology Initiatives (MISTI) Funds; the Ministry of Science and Technology (MOST) of Taiwan (103-2119-M-001-010-MY2, 105-2112-M-001-025-MY3, 105-2119-M-001-042, 106-2112-M-001-011, 106-2119-M-001-013, 106-2119-M-001-027, 106-2923-M-001-005, 107-2119-M-001-017, 107-2119-M-001-020, 107-2119-M-001-041, 107-2119-M-110-005, 107-2923-M-001-009, 108-2112-M-001-048, 108-2112-M-001-051, 108-2923-M-001-002, 109-2112-M-001-025, 109-2124-M-001-005, 109-2923-M-001-001, 110-2112-M-001-033, 110-2124-M-001-007 and 110-2923-M-001-001); the National Science and Technology Council (NSTC) of Taiwan (111-2124-M-001-005, 112-2124-M-001-014, 112-2112-M-003-010-MY3, and 113-2124-M-001-008); the Ministry of Education (MoE) of Taiwan Yushan Young Scholar Program; the Physics Division, National Center for Theoretical Sciences of Taiwan; the National Aeronautics and Space Administration (NASA, Fermi Guest Investigator grant 80NSSC23K1508, NASA Astrophysics Theory Program grant 80NSSC20K0527, NASA NuSTAR award 80NSSC20K0645); NASA Hubble Fellowship Program Einstein Fellowship; NASA Hubble Fellowship grants HST-HF2-51431.001-A, HST-HF2-51482.001-A, HST-HF2-51539.001-A, HST-HF2-51552.001A awarded by the Space Telescope Science Institute, which is operated by the Association of Universities for Research in Astronomy, Inc., for NASA, under contract NAS5-26555; the National Institute of Natural Sciences (NINS) of Japan; the National Key Research and Development Program of China (grant 2016YFA0400704, 2017YFA0402703, 2016YFA0400702); the National Science and Technology Council (NSTC, grants NSTC 111-2112-M-001 -041, NSTC 111-2124-M-001-005, NSTC 112-2124-M-001-014); the US National Science Foundation (NSF, grants AST-0096454, AST-0352953, AST-0521233, AST-0705062, AST-0905844, AST-0922984, AST-1126433, OIA-1126433, AST-1140030, DGE-1144085, AST-1207704, AST-1207730, AST-1207752, MRI-1228509, OPP-1248097, AST-1310896, AST-1440254, AST-1555365, AST-1614868, AST-1615796, AST-1715061, AST-1716327, AST-1726637, OISE-1743747, AST-1743747, AST-1816420, AST-1935980, AST-1952099, AST-2034306, AST-2205908, AST-2307887, AST-2407810); NSF Astronomy and Astrophysics Postdoctoral Fellowship (AST-1903847); the Natural Science Foundation of China (grants 11650110427, 10625314, 11721303, 11725312, 11873028, 11933007, 11991052, 11991053, 12192220, 12192223, 12273022, 12325302, 12303021); the Natural Sciences and Engineering Research Council of Canada (NSERC); the National Research Foundation of Korea (the Global PhD Fellowship Grant: grants NRF-2015H1A2A1033752; the Korea Research Fellowship Pro-

gram: NRF-2015H1D3A1066561; Brain Pool Program: RS-2024-00407499; Basic Research Support Grant 2019R1F1A1059721, 2021R1A6A3A01086420, 2022R1C1C1005255, RS-2022-NR071771, RS-2025-16067786); the POSCO Science Fellowship of the POSCO TJ Park Foundation; NOIRLab, which is managed by the Association of Universities for Research in Astronomy (AURA) under a cooperative agreement with the National Science Foundation; the A.G. Leventis Foundation; Onsala Space Observatory (OSO) national infrastructure, for the provisioning of its facilities/observational support (OSO receives funding through the Swedish Research Council under grant 2017-00648); the Perimeter Institute for Theoretical Physics (research at Perimeter Institute is supported by the Government of Canada through the Department of Innovation, Science and Economic Development and by the Province of Ontario through the Ministry of Research, Innovation and Science); the Portuguese Foundation for Science and Technology (FCT) grants (Individual CEEC program – 5th edition, CIDMA through the FCT Multi-Annual Financing Program for R&D Units UID/04106, CERN/FIS-PAR/0024/2021, 2022.04560.PTDC); the Princeton Gravity Initiative; the Spanish Ministerio de Ciencia, Innovación y Universidades (grants PID2022-140888NB-C21, PID2022-140888NB-C22, PID2023-147883NB-C21, RYC2023-042988-I); the Severo Ochoa grant CEX2021-001131-S funded by MICIU/AEI/10.13039/501100011033; The European Union's Horizon Europe research and innovation program under grant agreement No. 101093934 (RADIOBLOCKS); The European Union "NextGenerationEU", the Recovery, Transformation and Resilience Plan, the CUII of the Andalusian Regional Government and the Spanish CSIC through grant AST22_00001_Subproject_10; "la Caixa" Foundation (ID 100010434) through fellowship codes LCF/BQ/DI22/11940027 and LCF/BQ/DI22/11940030; the University of Pretoria for financial aid in the provision of the new Cluster Server nodes and SuperMicro (USA) for a SEEDING GRANT approved toward these nodes in 2020; the Shanghai Municipality orientation program of basic research for international scientists (grant no. 22JC1410600); the Shanghai Pilot Program for Basic Research, Chinese Academy of Science, Shanghai Branch (JCYJ-SHFY-2021-013); the Simons Foundation (grant 00001470); the Spanish Ministry for Science and Innovation grant CEX2021-001131-S funded by MCIN/AEI/10.13039/501100011033; the Spinoza Prize SPI 78-409; the South African Research Chairs Initiative, through the South African Radio Astronomy Observatory (SARAO, grant ID 77948), which is a facility of the National Research Foundation (NRF), an agency of the Department of Science and Innovation (DSI) of South Africa; the Swedish Research Council (VR); the Taplin Fellowship; the Toray Science Foundation; the UK Science and Technology Facilities Council (grant no. ST/X508329/1); the US Department of Energy (USDOE) through the Los Alamos National Laboratory (operated by Triad National Security, LLC, for the National Nuclear Security Administration of the USDOE, contract 89233218CNA000001); and the YCAA Prize Postdoctoral Fellowship. This work was also supported by the National Research Foundation of Korea (NRF) grant funded by the Korea government(MSIT) (RS-2024-00449206). We acknowledge support from the Coordenação de Aperfeiçoamento de Pessoal de Nível Superior (CAPES) of Brazil through PROEX grant number 88887.845378/2023-00. We acknowledge financial support from Millenium Nucleus NCN23_002 (TITANs) and Comité Mixto ESO-Chile. We thank the staff at the participating observatories, correlation centers, and institutions for their enthusiastic support. This paper makes use of the following ALMA data: ADS/JAO.ALMA#2017.1.00841.V and ADS/JAO.ALMA#2019.1.01797.V. ALMA is a partnership of the European Southern Observatory (ESO; Europe, representing its member states), NSF, andNational Institutes of Natural Sciences of Japan, together with National Research Council (Canada), Ministry of Science and Technology (MOST; Taiwan), Academia Sinica Institute of Astronomy and Astrophysics (ASIAA; Taiwan), and Korea Astronomy and Space Science Institute (KASI; Republic of Korea), in cooperation with the Republic of Chile. The Joint ALMA Observatory is operated by ESO, Associated Universities, Inc. (AUI)/NRAO, and the National Astronomical Observatory of Japan (NAOJ). The NRAO is a facility of the NSF operated under cooperative agreement by AUI. This research used resources of the Oak Ridge Leadership Computing Facility at the Oak Ridge National Laboratory, which is supported by the Office of Science of the U.S. Department of Energy under contract No. DE-AC05-00OR22725; the ASTROVIVES FEDER infrastructure, with project code IDIFEDER-2021-086; the computing cluster of Shanghai VLBI correlator supported by the Special Fund for Astronomy from the Ministry of Finance in China. We also thank the Center for Computational Astrophysics, National Astronomical Observatory of Japan. This work was supported by FAPESP (Fundacao de Amparo a Pesquisa do Estado de Sao Paulo) under grant 2021/01183-8. APEX is a collaboration between the Max-Planck-Institut für Radioastronomie (Germany), ESO, and the Onsala Space Observatory (Sweden). The SMA is a joint project between the SAO and ASIAA and is funded by the Smithsonian Institution and the Academia Sinica. The JCMT is operated by the East Asian Observatory on behalf of the NAOJ, ASIAA, and KASI, as well as the Ministry of Finance of China, Chinese Academy of Sciences, and the National Key Research and Development Program (No. 2017YFA0402700) of China and Natural Science Foundation of China grant 11873028. Additional funding support for the JCMT is provided by the Science and Technologies Facility Council (UK) and participating universities in the UK and Canada. The LMT is a project operated by the Instituto Nacional de Astrófisica, Óptica, y Electrónica (Mexico) and the University of Massachusetts at Amherst (USA). The IRAM 30 m telescope on Pico Veleta, Spain and the NOEMA interferometer on Plateau de Bure, France are operated by IRAM and supported by CNRS (Centre National de la Recherche Scientifique, France), MPG (Max-Planck-Gesellschaft, Germany), and IGN (Instituto Geográfico Nacional, Spain). The SMT is operated by the Arizona Radio Observatory, a part of the Steward Observatory of the University of Arizona, with financial support of operations from the State of Arizona and financial support for instrumentation development from the NSF. Support for SPT participation in the EHT is provided by the National Science Foundation through award OPP-1852617 to the University of Chicago. Partial support is also provided by the Kavli Institute of Cosmological Physics at the University of Chicago. The SPT hydrogen maser was provided on loan from the GLT, courtesy of ASIAA. This work used the Extreme Science and Engineering Discovery Environment (XSEDE), supported by NSF grant ACI-1548562, and CyVerse, supported by NSF grants DBI-0735191, DBI-1265383, and DBI-1743442. XSEDE Stampede2 resource at TACC was allocated through TG-AST170024 and TG-AST080026N. XSEDE JetStream resource at PTI and TACC was allocated through AST170028. This research is part of the Frontera computing project at the Texas Advanced Computing Center through the Frontera Large-Scale Community Partnerships allocation AST20023. Frontera is made possible by National Science Foundation award OAC-1818253. This research was done using services provided by the OSG Consortium (Pordes & Petravick 2007; Sfiligoi et al. 2009), which is supported by the National Science Foundation award Nos. 2030508 and 1836650. Additional work used ABACUS2.0, which is part of the eScience center at Southern Denmark University, and the Kultrun Astronomy Hybrid Cluster (projects Conicyt Programa de Astronomia Fondo Quimal QUIMAL170001, Conicyt PIA ACT172033, Fondecyt Iniciacion 11170268, Quimal 220002). Simulations were also performed on the SuperMUC cluster at the LRZ in Garching, on the LOEWE cluster in CSC in Frankfurt, on the HazelHen cluster at the HLRS in Stuttgart, and on the Pi2.0 and Siyuan Mark-I at Shanghai Jiao Tong University. The computer resources of the Finnish IT Center for Science (CSC) and the Finnish Computing Competence Infrastructure (FCCI) project are acknowledged. This research was enabled in part by support provided by Compute Ontario (http://computeontario.ca), Calcul Quebec (http://www.calculquebec.ca), and the Digital Research Alliance of Canada (https://alliancecan.ca/en). The EHTC has received generous donations of FPGA chips from Xilinx Inc., under the Xilinx University Program. The EHTC has benefited from technology shared under open-source license by the Collaboration for Astronomy Signal Processing and Electronics Research (CASPER). The EHT project is grateful to T4Science and Microsemi for their assistance with hydrogen masers. This research has made use of NASA's Astrophysics Data System. We gratefully acknowledge the support provided by the extended

staff of the ALMA, from the inception of the ALMA Phasing Project through the observational campaigns of 2017 and 2018. We would like to thank A. Deller and W. Brisken for EHT-specific support with the use of DiFX. We thank Martin Shepherd for the addition of extra features in the Difmap software that were used for the CLEAN imaging results presented in this paper. We acknowledge the significance that Maunakea, where the SMA and JCMT EHT stations are located, has for the indigenous Hawaiian people.

The *Fermi* LAT Collaboration acknowledges generous ongoing support from a number of agencies and institutes that have supported the development and operation of the LAT as well as scientific data analysis. These include the National Aeronautics and Space Administration and the Department of Energy in the United States, the Commissariat í l'Energie Atomique and the Centre National de la Recherche Scientifique / Institut National de Physique Nucléaire et de Physique des Particules in France, the Agenzia Spaziale Italiana and the Istituto Nazionale di Fisica Nucleare in Italy, the Ministry of Education, Culture, Sports, Science and Technology (MEXT), High Energy Accelerator Research Organization (KEK) and Japan Aerospace Exploration Agency (JAXA) in Japan, and the K. A.Wallenberg Foundation, the Swedish Research Council and the Swedish National Space Board in Sweden. Additional support for science analysis during the operations phase is gratefully acknowledged from the Istituto Nazionale di Astrofisica in Italy and the Centre National d'Etudes Spatiales in France. This work is performed in part under DOE Contract DE-AC02-76SF00515.

This research has made use of data obtained with the Global Millimeter VLBI Array (GMVA), which consists of telescopes operated by the MPIfR, IRAM, Onsala, Metsahovi, Yebes, the Korean VLBI Network, the Greenland Telescope, the Green Bank Observatory and the Very Long Baseline Array (VLBA). The VLBA and the GBT are facilities of the National Science Foundation operated under cooperative agreement by Associated Universities, Inc. The data were correlated at the correlator of the MPIfR in Bonn, Germany.

We would like to thank the Instituto de Astrofísica de Canarias for the excellent working conditions at the Observatorio del Roque de los Muchachos in La Palma. The financial support of the German BMFTR, MPG and HGF; the Italian INFN and INAF; the Swiss National Fund SNF; the grants PID2022-136828NB-C41, PID2022-137810NB-C22, PID2022-138172NB-C41, PID2022-138172NB-C42, PID2022-138172NB-C43, PID2022-139117NB-C41, PID2022-139117NB-C42, PID2022-139117NB-C43, PID2022-139117NB-C44, CNS2023-144504 funded by the Spanish MCIN/AEI/ 10.13039/501100011033 and "ERDF A way of making Europe"; the Indian Department of Atomic Energy; the Japanese ICRR, the University of Tokyo, JSPS, and MEXT; the Bulgarian Ministry of Education and Science, National RI Roadmap Project DO1-400/18.12.2020 and the Academy of Finland grant nr. 320045 is gratefully acknowledged. This work has also been supported by Centros de Excelencia "Severo Ochoa" y Unidades "María de Maeztu" program of the Spanish MCIN/AEI/ 10.13039/501100011033 (CEX2019-000918-M, CEX2021-001131-S, CEX2024001442-S), by AST22_00001_9 with funding from NextGenerationEU funds and by the CERCA institution and grants 2021SGR00426, 2021SGR00607 and 2021SGR00773 of the Generalitat de Catalunya; by the Croatian Science Foundation (HrZZ) Project IP-2022-10-4595 and the University of Rijeka Project uniriprirod-18-48; by the Deutsche Forschungsgemeinschaft (SFB1491) and by the Lamarr-Institute for Machine Learning and Artificial Intelligence; by the Polish Ministry of Science and Higher Education grant No. 2025/WK/04; by the European Union (ERC, MicroStars, 101076533); and by the Brazilian MCTIC, the CNPq Productivity Grant 309053/2022-6 and FAPERJ Grants E-26/200.532/2023 and E-26/211.342/2021.

We thank the H.E.S.S. Collaboration for providing the H.E.S.S. data that have been analysed for this publication.

Appendix B: Observations description

This section provides a detailed description of the MWL observations carried out during the EHT campaigns on 3C 279 in April 2017. The measurements contributing to the quasi-simultaneous spectrum of 3C 279 in 2017 (see Fig. 5) are summarized in Table C.1.

B.1. Radio observations

B.1.1. RadioAstron - 18 and 6 cm space VLBI

RadioAstron was a mission comprising a parabolic 10-m Space Radio Telescope on a highly elliptical orbit around Earth, observing together with ground-based radio telescopes. 3C 279 was monitored during the RadioAstron mission (Kardashev et al. 2017) at wavelengths $\lambda = 18$ cm (1.7 GHz; 58 fringe detections on space-ground baselines longer than 1 Earth diameter), $\lambda = 6$ cm (4.8 GHz; 226 detections), and $\lambda = 1.3$ cm (22 GHz; 9 detections). In the period 2016–2018, there were 7 and 12 non-imaging experiments conducted at 18 cm and 6 cm delivering, in total, 13 and 17 space-ground fringe detections, respectively. The longest baseline with fringe detection was 25.3 Earth diameters (1.8 Gλ, 322599 km) at 18 cm and 23.2 Earth diameters (4.8 Gλ, 295390 km) at 6 cm.

At 18 cm, the ground network of participating telescopes consisted of Effelsberg (100 m), Green Bank (110 m), Hartbeesthoek (26 m), Mopra (22 m), Medicina (32 m), Torun (32 m), and Irbene (16 m). The first four provided fringe detections on the baselines with the space antenna. At 6 cm, participating antennas included Effelsberg, Hartbeesthoek, Torun, Mopra, Badary (32 m), Warkworth (30 m), Noto (30 m), Westerbork (single antenna, 25 m), and Irbene. The first five provided fringe detections with the space antenna.

The amplitude of the signal was calibrated using system temperatures measured at individual telescopes. All subsequent analysis of RadioAstron data was performed with amplitude data only. At both frequencies, we fitted measured amplitudes using three Gaussian components. Due to a scarcity of ground-space fringe detections, we combined all the data taken between 2016 and 2018. The robustness of fits and uncertainty estimates were performed using bootstrapping. In each of 1000 realizations, a random 10% of the data was removed and the fitting procedure was performed again.

Parameters of the Gaussian model components are provided in Table B.1. Since we used only amplitudes, we can robustly constrain only size and flux of the components, but not their relative positions. However, at both wavelengths, it is clear that the largest components (c1 and l1) describe extended jet, the next ones (c2 and l2) describe the overall VLBI core, while the smallest and the dimmest ones (c3 and l3) describe some fine structure within the cores. These components show the highest observed brightness temperature, surpassing that of the core. This can indicate the presence of more energetic particles emitting in these regions, which might be associated with either a fast jet spine or regions of particle re-acceleration. It should be noted that even the core is located well downstream of the central black hole, at distances as great as tens of parsecs.

B.1.2. VLBA

VLBA 2 cm-VLBI Very Long Baseline Array (VLBA) total and polarized intensity images at a wavelength of 2 cm were obtained from the MOJAVE program[4] (Lister et al. 2018). A VLBA 15 GHz image from 2017 Apr 22, quasi-simultaneous with our campaign, is shown in Fig. B.1.

[4] https://www.cv.nrao.edu/MOJAVE/

Table B.1. Gaussian components fitted to 2016-2018 ground-space VLBI imaging data including RadioAstron at 6 cm and 18 cm.

Comp	Flux [Jy]	Size FWHM [mas]	T_b [K]
	6 cm		
c1	5.19 ± 0.49	3.3 ± 0.8	$(2.3 \pm 1.2) \times 10^{10}$
c2	3.86 ± 0.25	0.21 ± 0.01	$(3.4 \pm 0.5) \times 10^{12}$
c3	0.46 ± 0.03	0.11 ± 0.03	$(8.0 \pm 0.9) \times 10^{12}$
	18 cm		
l1	10.53 ± 0.16	22.1 ± 0.4	$(9.5 \pm 0.4) \times 10^{9}$
l2	3.37 ± 0.08	0.5 ± 0.0	$(5.1 \pm 0.4) \times 10^{12}$
l3	0.32 ± 0.06	0.1 ± 0.0	$(6.5 \pm 1.9) \times 10^{12}$

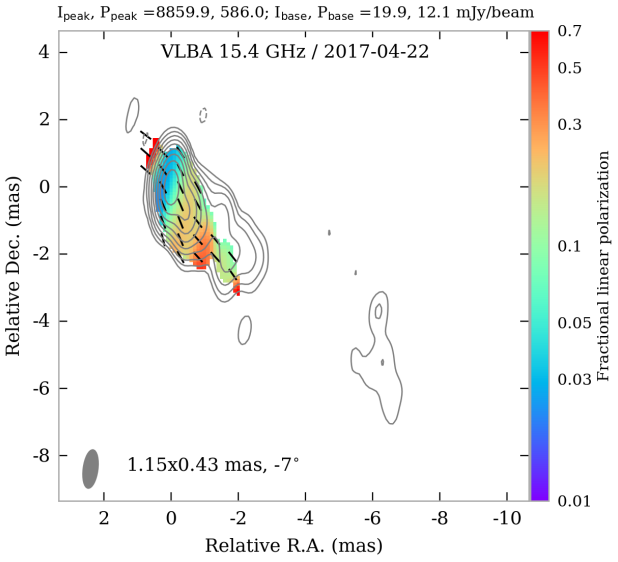


Fig. B.1. VLBA MOJAVE linear (contours) and polarized (color scale) intensity image at 15 GHz of the 3C 279 jet on April 22, 2017. Black line segments indicate orientation of polarization vectors (not corrected for Faraday rotation).

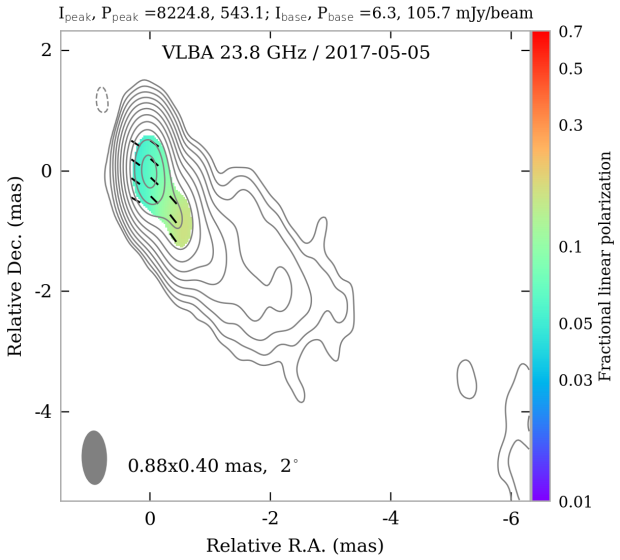


Fig. B.2. VLBA naturally weighted image at 1.2 cm (24 GHz) of the 3C 279 jet from May 5, 2017. Black line segments indicate orientation of polarization vectors (not corrected for Faraday rotation).

Table B.2. Parameters of the 43 GHz images presented in Figure 3.

Date	MJD	I-peak [Jy/beam]	Beam [mas^2]	Beam PA [deg]	RMS [mJy/beam]
(1)	(2)	(3)	(4)	(5)	(6)
Feb. 4	57788	6.56	0.50×0.14	−11.5	6
Mar. 19	57831	5.46	0.39×0.16	−4.5	6
Apr. 16	57859	5.79	0.42×0.16	−10.1	4
May 13	57886	9.36	0.37×0.15	−4.6	16
Jun. 8	57912	10.5	0.39×0.15	−4.9	9

VLBA - 1.2 cm VLBI 3C 279 was used as a calibrator for a VLBA observation (program BG251A) at 1.2 cm (24 GHz) on May 5, 2017.The detailed description of the observational setup and calibration procedures is given in Kravchenko et al. (2020). The total and linearly polarized intensity image is displayed in Fig. B.2.

VLBA - 7 mm VLBI VLBA observations at 7 mm (43 GHz) included in the present study were obtained within the VLBA-BU-BLAZAR program[5] (Jorstad et al. 2017) with a roughly monthly cadence from February 4 to June 8, 2017. The parameters of the maps shown in Fig. 3 are given in Table B.2 as follows: 1 - epoch of observation; 2 - MJD; 3 - total intensity peak; 4 - beam size; 5 - beam position angle; 6 - total intensity noise level.

B.1.3. KVN - 13.6, 7, 3.5 and 2.3 mm VLBI

3C 279 was monitored with the KVN as part of the Interferometric Monitoring of GAmma-ray Bright Active galactic nuclei (iMOGABA Lee et al. 2016) program. This consisted of monthly, simultaneous 22, 43, 86, and 129 GHz, single polarization (LCP) observations. The data were calibrated using a modified version of the KVN pipeline (Hodgson et al. 2016; EHT MWL Science Working Group et al. 2024). We coherently averaged the 22 and 43 GHz data data over 30 seconds, whereas we averaged the 86 and 129 GHz data over 10 seconds prior to imaging. Imaging and phase-only self calibration were conducted in `Difmap` (Shepherd 1997). Afterwards, the CLEAN components within a 2 mas field of view of the core were summed to obtain the compact flux density at 22 and 43 GHz. At 86 and 129 GHz, the CLEAN components within a 1 mas field of view were used. Uncertainties of 10, 20, and 30% were adopted for the flux density measurements at 43, 86, and 129 GHz, respectively. Uncertainties of 10% to 15% were adopted for measurements at 22 GHz, depending on whether the specific observation was affected by additional flux loss (EHT MWL Science Working Group et al. 2024).

KVN multi-frequency (22, 43, 86, and 129 GHz) observations of the milliarcsecond-scale core reveal flux density variability, with the emission increasing during April–May (see Fig. B.3).

[5] www.bu.edu/blazars/BEAM-ME.html

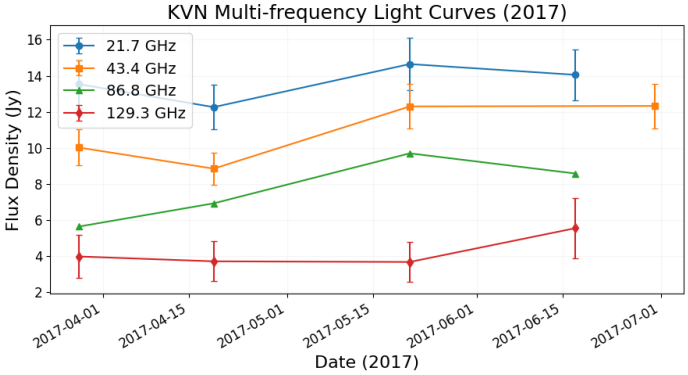


Fig. B.3. KVN multi-frequency light curves showing flux density variations observed between March and June 2017.

B.1.4. GMVA - 3 mm VLBI

Quasi-simultaneous observations with the Global Millimeter VLBI Array (GMVA) were conducted on April 1 2017, as part of the GMVA blazar monitoring program[6].The resulting image of the source is presented in the middle panel of Fig. 2.

B.1.5. ALMA - 3.3, 2.9, 1.3 and 0.8 mm

Archival observations of 3C 279 with the Atacama Large Millimeter/submillimeter Array (ALMA) at 91.5, 103.5, 233, and 343 GHz were obtained from Goddi et al. (2021) and from the ALMA Calibrator Source Catalogue[7].

B.1.6. SMA - 1.3 and 0.8 mm

Light curves of 3C 279 at 1.3 mm and 0.8 mm (230 and 345 GHz) with the Submillimeter Aray (SMA) were obtained from the SMA calibrator list[8].

B.1.7. EHT - 1.3 mm VLBI

The source 3C 279 was observed in 2017 by the EHT array on April 5, 6, 10, and 11. Details of the observations, calibration, and imaging can be found from (EHT Collaboration 2019b,c), and (EHT Collaboration 2019d). The source image on April 11 is shown in the rightmost panel of Fig. 2.

B.2. Optical-UV data

B.2.1. Kanata/HONIR

The HONIR instrument (Akitaya et al. 2014), mounted on the Kanata telescope at the Higashi-Hiroshima Observatory, was used for the observations. Standard data reduction procedures were applied, including bias or dark subtraction, flat-field correction, removal of cosmic-ray contamination, sky-background subtraction, and stacking of the images to improve the signal-to-noise ratio. Photometric magnitudes of the target were measured through an aperture photometry using `SExtractor` (Bertin & Arnouts 1996). The typical image size of a point source, defined by the full width at half maximum (FWHM) of its point spread function, ranged from 1–3″ depending on observational conditions. The aperture diameter was set to 2.8 times the FWHM. Object fluxes were converted to magnitudes by comparison with nearby stars, using the Pan-STARRS1 catalog (Flewelling et al. 2020) for optical bands (after filter conversion; Tonry et al. 2012) and the 2MASS catalog (Skrutskie et al. 2006) for NIR bands, with corrections for Galactic extinction (Schlafly & Finkbeiner 2011). HONIR provides independent linear polarization components, split by a Wollaston prism, with a half-wave plate (HWP) in front to rotate the plane of polarization. Four pairs of polarized images in R_C and J bands were obtained at HWP angles of 0°, 45°, 22.5°, and 67.5°. Integrated target fluxes were measured via aperture photometry, and normalized Stokes parameters were calculated following Kawabata et al. (1999).

B.2.2. Optical Photometric and Polarimetric Data

Optical polarization observations of 3C 279 in R band, along with photometric estimates, were carried out during the EHT 2017 campaign at four telescopes: the 1.8 m Perkins telescope (PTO, Flagstaff, AZ, USA), the 40 cm LX-200 telescope (St.Petersburg, Russia), the 70 cm AZT-8 telescope (Crimea Astrophysical Obs.), and the 1.54 m Kuiper telescope (Steward Obs., Tuscon, AZ, USA). The Perkins telescope is equipped with the PRISM camera, which includes a polarimeter with a rotating half-wave plate. For details of observations and data reduction see Jorstad et al. (2010). Polarization observations at the LX-200 and AZT-8 telescopes were performed in the same manner, each using an identical photometer-polarimeter, with two Savart plates rotated by 45° relative to each other. Swapping the plates allows one to obtain a normalized Stokes parameter, either q or u (for more detail see Larionov et al. 2008). Observations at the Kuiper telescope were performed using the CCD Imaging and Spectro-polarimeter (Schmidt et al. 1992), yielding spectra that span the range of 4000–7550 Å with a dispersion of 4 Å per pixel. In polarization mode, full-resolution Stokes spectra were obtained to calculate the linear polarization parameters within 5000–7000 Å, close to R band. Details of the spectropolarimetric data reduction can be found in Smith (2016).

Photometric measurements of 3C 279 were also obtained between 2015 and 2024 using optical and near-infrared bandpass filters: V and R_C bands from the Johnson-Cousins photometric system, and J and K_S bands from the Mauna Kea Observatories Near-Infrared photometric system (Tokunaga et al. 2002).

B.2.3. Swift-UVOT

The UV–Optical Telescope (UVOT, Roming et al. 2005) of the Neil Gehrels *Swift* Observatory provides UV and optical data in 6 bands - uvw1, uvm2, uvw2, u, b, and v. We retrieved the data from the *Swift* Archive and reduced them with v6.31.1 of the `HEAsoft` software and CALDB v20221216. For photometric analysis we used a 5″ circular region centered on the source and a 20″ circular aperture on a source-free region of the image to represent the background and processed the data with the `uvotsource` task, setting the detection significance level to 5σ. None of the observations suffered a high coincidence loss. We used the count-rate-to-flux conversion factors reported by Breeveld et al. (2011) for γ-ray burst models, which correspond to continuum spectra similar to those of blazars. For the UV data, we de-reddened the magnitudes using the Fitzpatrick (1999) interstellar extinction curve with an R_v=3.1 and A_λ values from

[6] https://www.bu.edu/blazars/vlbi3mm/index.html
[7] https://almascience.eso.org/alma-data/calibrator-catalogue
[8] http://sma1.sma.hawaii.edu/callist/callist.html?data=1256-057

Schlafly & Finkbeiner (2011). Optical magnitudes were corrected for Galactic extinction using the Schlafly & Finkbeiner (2011) values. The derived UVOT flux densities obtained during the EHT 2017 campaign are plotted in Fig. 4.

B.3. X-ray observations: Swift-XRT

During the 2017 EHT campaign we obtained measurements with the Neil Gehrels *Swift* Observatory X-ray Telescope (XRT, Burrows et al. 2005) over the 0.3-10 keV photon energy range. The observations during the 2017 campaign were mostly quasi-simultaneous, on March 26 and 27 and on April 8, 12, and 13. All observations were made in photon counting mode. We used v6.31.1 of the `HEAsoft` package and CALDB v20221216 to process the data. A circular source region with a 50″ radius and an annular background region with inner radius 75″ and outer radius 100″, both centered on 3C 279, were employed for data processing. The latter includes: cleaning the data, creating an exposure map with the `xrtpipeline` tool, extracting the image and spectra using `XSELECT`, and generating the ancillary response file with `xrtmkarf`. We used Cash statistics (Cash 1979; Humphrey et al. 2009) in the form of the modified C-statistic `cstat` to fit the data in `XSPEC`, and grouped the data by single photons in `grppha`. The spectrum was then fit in `XSPEC` using an absorbed simple power law with Galactic column density $N_{\rm H} = 2.2\times10^{20}$ cm^{-2}, as provided by the NASA HEASARC TOOL page.

Figure 4 presents derived fluxes of 3C 279 at 0.3-10 keV. The spectral fit yields a photon index of $\Gamma = 1.5 \pm 0.1$ during the 2017 EHT campaign. In particular, for the observations performed on April 8 (MJD 57851.7), which were used for the spectral modeling, the source presents a photon flux of $\Phi = (5.01 \pm 0.57) \times 10^{-3}$ ph cm^2 s^{-1} and a photon index of $\Gamma = 1.46 \pm 0.19$.

B.4. Gamma-ray data

B.4.1. *Fermi*-LAT observations

The *Fermi*-LAT analysis of γ-ray emission of the blazar 3C 279, presented in this work, was perfomed using 16 years of observations (2008 August 4–2024 August 4) and, separately with higher time resolution, a 1,5-month interval around the 2017 EHT campaign (March 15 – April 30, 2017). We selected P8R3 source class events (Bruel et al. 2018) within a 15° ROI centered on 3C 279, restricting the energy range to 100 MeV–1 TeV for optimal data quality (although the source is detected also below 100 MeV; Principe et al. 2018). The analysis, including model optimization, search for new sources, source localization, spectral, and variability studies, was carried out with `Fermipy`[9] (Wood et al. 2017) (v1.3.1) and the P8R3_Source_V3 IRFs. Maps were produced with 0.1° pixels. To minimize contamination from Earth-limb emission (Abdo et al. 2009), below 300 MeV we excluded events with zenith angles $z > 85°$ and photons from PSF0 and PSF1 event types. Between 300 MeV and 1 GeV we excluded events with $z > 85°$ and photons from the PSF0 event type. While above 1 GeV we used all events with $z < 105°$. The model included all 4FGL-DR4 sources (Abdollahi et al. 2020, 2022) within 20° of 3C 279, along with Galactic diffuse and isotropic emission templates[10]. The spectral normalization parameter was left free for sources within 4°, while it was kept fixed otherwise. The spectral index was freed for sources within 2° and fixed otherwise. For variability studies during March-April 2017, the data were binned into 3-hour intervals. Light curves were derived by fixing the photon index to the 16-year best-fit value and allowing only the normalization to vary; 95% upper limits were computed for bins with $< 3\sigma$ significance. The source localization analysis yielded a highly significant ($> 500\sigma$) detection at (R.A., dec.) = (194.045° ± 0.001°, −5.788° ± 0.001°), with $R_{95} = 0.003°$, consistent with 4FGL J1256.1−0547 (4FGL-DR4), identified as 3C 279. The γ-ray spectrum of 3C 279 was modeled using a log-parabolic function, as adopted in the 4FGL catalog for the entire 16-year dataset and for the periods of April 5–11, 2017, and April 5–6, 2017.

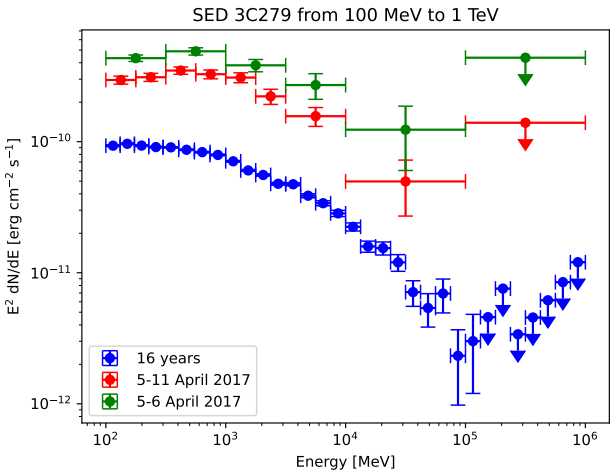


Fig. B.4. 3C 279 SED from *Fermi*-LAT obtained using 16 years (2008 August 4–2024 August 4, blue points), the data of April 5-11, 2017 (red points), and April 5-6, 2017 (green points). A 1-σ upper limit is reported for bins with $< 3\sigma$ significance.

Figure B.4 presents the SED derived from 16 years of *Fermi*-LAT observations, along with the SED for April 5-11, 2017, contemporaneous with the EHT campaign. The γ-ray emission variability of 3C 279 (see the two light curves reported in Fig. 4 and Fig. B.5) indicates that the source was in a high-activity state during the EHT observing campaign. Specifically, contemporaneous with the first two EHT observations, 3C 279 exhibited enhanced emission between April 5 and 6, reaching a flux of $\phi_{\rm April\,5-6, E>100\,MeV} = (2.90\pm0.12)\times10^{-6}$ ph cm^{-2} s^{-1}. Following this peak, the flux declined to a level consistent with the 16-year *Fermi*-LAT average of $\phi_{\rm 2008-2024, E>100\,MeV} = (6.32\pm0.03)\times10^{-7}$ ph cm^{-2} s^{-1}. Moreover, during the raising phase of the flaring episode a record optical flare occurred (see Sect. 3.2).

B.4.2. H.E.S.S. observations

The High Energy Stereoscopic System (H.E.S.S.) is a hybrid array of Imaging Atmospheric Cherenkov Telescopes (IACTs) located in the Khomas Highlands in Namibia, at an altitude of about 1800 m above sea level. It is composed of four (CT1-4) Cherenkov telescopes of 12 m diameter that have been observing the VHE γ-ray sky for more than 20 years, complemented by a fifth 28 m telescope (CT5) since 2012. The H.E.S.S. array has a sensitivity of ∼1% of Crab Nebula's flux above

[9] http://fermipy.readthedocs.io/en/latest/
[10] https://fermi.gsfc.nasa.gov/ssc/data/access/lat/BackgroundModels.html

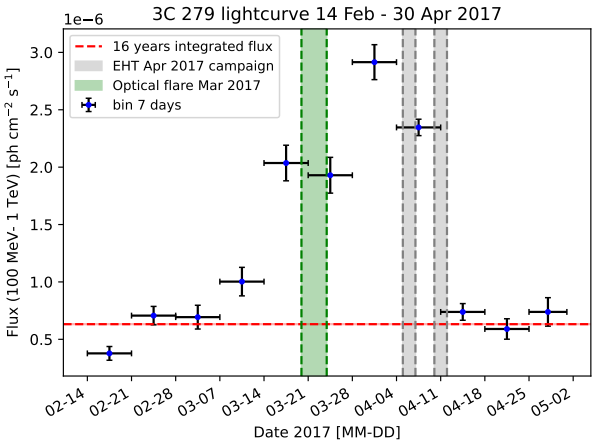


Fig. B.5. *Fermi*-LAT 7-day binned light curve of 3C 279 between February 14 and April 30, 2017. The dashed red line represents the 16-year-averaged flux $\phi_{E>100\,\mathrm{MeV}} = (6.32 \pm 0.03) \times 10^{-7}$ ph cm^{-2} s^{-1}. The vertical green band indicates the duration of the record optical flare, and the vertical gray bands mark the EHT observing dates.

100 GeV, over 25 h of observations under low zenith angles (∼20°) (Aharonian et al. 2006).

H.E.S.S. observed 3C 279 during the night of March 24 to 25, 2017, which constitutes the closest H.E.S.S. observation epoch to the 2017 coordinated EHT-MWL campaign. Only data from the CT1-4 telescopes could be analyzed, since CT5 suffered from hardware problems throughout the entire observation night. The analysis was performed using two independent techniques: *Model analysis* (de Naurois & Rolland 2009) and Image Pixel-wise fit for Atmospheric Cherenkov Telescopes (*ImPACT*) (Parsons & Hinton 2014) chains, which agreed with each other. High-level data products containing already reconstructed events and Instrument Response Functions were processed using *Gammapy* (Donath et al. 2023)(version 1.2)[11]. Moreover, contrary to the usual "wobble" observing mode, which permits simultaneous background measurements (Berge et al. 2007), the late March 2017 observations were taken directly on the source position, requiring 3D background subtraction, for which a template background model was generated using the BAccMod module[12].

3C 279 was not detected in a total of ∼4.2 hours of livetime. Nightly-averaged flux upper limits were derived above 100 GeV (mean energy threshold of ∼105 GeV), at 95% confidence level, using a typical photon index of 4.0 (H.E.S.S. Collaboration 2019) and the likelihood profile method implemented in *Gammapy*. They are included in Fig. 4, while differential upper limits are presented in Fig. 5.

B.4.3. MAGIC observations

The Major Atmospheric Gamma Imaging Cherenkov (MAGIC) stereoscopic telescope system consists of two 17 m diameter IACTs located at the Roque de los Muchachos Observatory on the Canary Island of La Palma (28.7° N, 17.9° W), at an altitude of 2200 m above sea level. Designed to detect air Cherenkov showers initiated by γ rays, MAGIC is sensitive to energies ranging from approximately 50 GeV to 50 TeV. For low-zenith-angle observations ($15° < zd < 30°$), its sensitivity above 104 GeV is (1.445 ± 0.015) % of the Crab Nebula's flux over 50 h of observation for a point-like source (Aleksić et al. 2016).

The observations were performed in wobble mode, using 4 symmetrical positions w.r.t. the pointing position located 0.4° away from the source, allowing us to collect simultaneously the signal and background (Fomin et al. 1994). The observations presented in this work were taken during the 2017 campaign as reported in Table C.1. A total of 8.51 h were collected during 2017 after quality cuts. The observations were performed within a zenith angle range from 30° to 52°. The energy threshold of the analysis, calculated as the peak of the number of events for these observation conditions and a photon index of 4.0, is located at approximately 100 GeV. The analysis was performed using the standard MAGIC analysis framework MARS. A full description of the MAGIC analysis and systematic uncertainties estimation can be found in Aleksić et al. (2016) and references therein.

3C 279 was not detected above the standard 5 σ significance level in the VHE band by the MAGIC telescopes during the 2017 campaign. The nightly LC was derived, yielding a single flux data point with a significance of 2.5 σ. For the remaining nights, the measured significances were below 2 σ, and flux upper limits were therefore computed. The 95% confidence level U.L.s were calculated above an energy threshold of 100 GeV, defined as the peak of the event distribution, assuming a power-law spectral model with a photon index of 4.0, consistent with previous MAGIC detections of the source (MAGIC Collaboration 2008). The resulting light curve is shown in Fig. 4. A spectral analysis was also performed for the MWL SED. Since no significant VHE detection was achieved, only 95% confidence level upper limits are reported for energies above 74 GeV.

Appendix C: Quasi-simultaneous multi-wavelength spectrum

This section contains the MWL SED for the 3C 279 inner jet around the EHT observing campaign in 2017 (see Table C.1). To select the closest-in-time MWL data, the EHT observation on April 10 was adopted as a reference, since the only X-ray observation within the EHT observing window was on April 8. For the radio data included in the MWL SED, we considered the innermost region accessible at each observing frequency, corresponding either to the compact core alone (C0–0 component for the EHT; see Kim et al. 2020) or, for non-EHT observations, to the combined emission from the core and the inner jet.

[11] *Gammapy* is an open-source Python package for γ-ray data analysis (v. 1.2, https://doi.org/10.5281/zenodo.10726484)
[12] https://github.com/mdebony/BAccMod

Table C.1. Spectral Energy Distribution for 3C 279 during the 2017 EHT-MWL campaign.

Observatory	Band	ν [Hz]	Angular Scale[1] [″]	Obs. date [MJD]	Flux [Jy]	νF_ν [$\times 10^{-12}$ erg cm^{-2} s^{-1}]	Sect.
RadioAstron	1.67 GHz	1.67×10^9	5.0×10^{-4}	2016–2018	3.37 ± 0.08	$(5.63 \pm 0.14) \times 10^{-2}$	B.1.1.
RadioAstron	5 GHz	5×10^9	2.1×10^{-4}	2016–2018	3.86 ± 0.25	$(1.93 \pm 0.12) \times 10^{-1}$	B.1.1.
VLBA	15 GHz	1.5×10^{10}	1.0×10^{-3}	22-04-2017 / 57865	14.52 ± 1.25	2.18 ± 0.11	B.1.2.
VLBA	24 GHz	2.4×10^{10}	5.9×10^{-4}	05-05-2017 / 57878	7.15 ± 0.52	1.72 ± 0.13	B.1.2.
VLBA	43 GHz	4.3×10^{10}	1.3×10^{-4}	16-04-2017 / 57859	6.16 ± 0.49	2.65 ± 0.21	B.1.2.
KVN K	22 GHz	2.2×10^{10}	4.3×10^{-3}	18-04-2017 / 57861	12.25 ± 1.22	2.70 ± 0.27	B.1.3.
KVN Q	43 GHz	4.3×10^{10}	2.2×10^{-3}	18-04-2017 / 57861	8.84 ± 0.88	3.80 ± 0.38	B.1.3.
KVN W	86 GHz	8.6×10^{10}	1.1×10^{-3}	18-04-2017 / 57861	6.91 ± 0.69	5.94 ± 0.59	B.1.3.
KVN D	129 GHz	1.29×10^{11}	0.8×10^{-3}	18-04-2017 / 57861	3.69 ± 1.11	4.75 ± 1.43	B.1.3.
GMVA	86 GHz	8.6×10^{11}	2.0×10^{-4}	01-04-2017 / 57844	5.12 ± 0.77	4.42 ± 0.66	B.1.4.
ALMA	91.5 GHz	9.3×10^{10}	$\simeq 4$	04-04-2017 / 57847	12.93 ± 0.65	11.83 ± 0.60	B.1.5.
ALMA	103.5 GHz	1.03×10^{11}	$\simeq 3$	13-04-2017 / 57856	12.17 ± 0.7	12.59 ± 0.72	B.1.5.
ALMA	221 GHz	2.21×10^{11}	$\simeq 1$	06-04-2017 / 57849	9.36 ± 0.94	20.70 ± 2.10	B.1.5.
ALMA	343 GHz	3.43×10^{11}	$\simeq 0.4$	13–04-2017 / 57856	6.30 ± 0.07	21.61 ± 0.24	B.1.5.
SMA	235 GHz	2.35×10^{11}	~ 3	03-04-2017 / 57846	8.55 ± 0.45	20.1 ± 1.1	B.1.6.
SMA	261 GHz	2.61×10^{11}	~ 3	03-04-2017 / 57846	7.79 ± 0.45	20.3 ± 1.2	B.1.6.
EHT	230 GHz	2.3×10^{11}	2.4×10^{-5}	10-04-2017 / 57853	0.89 ± 0.05	2.05 ± 0.12	B.1.7.
Kanata	1220 nm	2.4×10^{14}	$\simeq 6$	22-03-2017 / 57834	$< 40.8 \times 10^{-3}$	< 97.9	B.2.1.
Kanata	658 nm	4.5×10^{14}	$\simeq 6$	22-03-2017 / 57834	$< 21.6 \times 10^{-3}$	< 97.2	B.2.1.
Kanata	551 nm	5.4×10^{14}	$\simeq 6$	18-03-2017 / 57830	$< 9.70 \times 10^{-3}$	< 52.4	B.2.1.
Perkins I	806 nm	3.7×10^{14}	$\simeq 3$	31-03-2017 / 57843	$(8.51 \pm 0.16) \times 10^{-3}$	31.7 ± 0.6	B.2.2.
Perkins R	658 nm	4.5×10^{14}	$\simeq 3$	31-03-2017 / 57843	$(6.15 \pm 0.07) \times 10^{-3}$	28.0 ± 0.3	B.2.2.
Perkins V	551 nm	5.4×10^{14}	$\simeq 3$	31-03-2017 / 57843	$(4.39 \pm 0.09) \times 10^{-3}$	23.9 ± 0.5	B.2.2.
Perkins B	445 nm	6.7×10^{14}	$\simeq 3$	31-03-2017 / 57843	$(2.98 \pm 0.10) \times 10^{-3}$	20.3 ± 0.7	B.2.2.
Swift-UVOT	546.8 nm	5.48×10^{14}	$\simeq 3$	14-04-2017 / 57857	$(1.16 \pm 0.09) \times 10^{-3}$	6.36 ± 0.49	B.2.3.
Swift-UVOT	439.2 nm	6.83×10^{14}	$\simeq 3$	14-04-2017 / 57857	$(8.56 \pm 0.41) \times 10^{-4}$	5.91 ± 0.28	B.2.3.
Swift-UVOT	346.5 nm	8.65×10^{14}	$\simeq 3$	27-04-2017 / 57839	$(1.00 \pm 0.04) \times 10^{-3}$	8.65 ± 0.35	B.2.3.
Swift-UVOT	260.0 nm	1.15×10^{15}	$\simeq 3$	14-04-2017 / 57857	$(4.32 \pm 0.22) \times 10^{-4}$	4.97 ± 0.25	B.2.3.
Swift-UVOT	224.6 nm	1.33×10^{15}	$\simeq 3$	14-04-2017 / 57857	$(3.22 \pm 0.19) \times 10^{-4}$	4.28 ± 0.25	B.2.3.
Swift-UVOT	192.8 nm	1.55×10^{15}	$\simeq 3$	14-04-2017 / 57857	$(2.84 \pm 0.12) \times 10^{-4}$	4.40 ± 0.19	B.2.3.
Swift-XRT	0.3-10 keV	4.19×10^{17}	$\simeq 75$	08-04-2017 / 57851	$(6.7 \pm 1.3) \times 10^{-72}$	15.8 ± 3.1[2]	B.3.
Fermi-LAT	0.1 - 0.18 GeV	3.22×10^{22}	$\simeq 7000$	05–11-04-2017 / 57848–57854	$(9.16 \pm 0.65) \times 10^{-10}$	295.5 ± 20.9	B.4.1.
Fermi-LAT	0.18 - 0.32 GeV	5.73×10^{22}	$\simeq 7000$	05–11-04-2017 / 57848–57854	$(5.41 \pm 0.38) \times 10^{-10}$	310.2 ± 21.9	B.4.1.
Fermi-LAT	0.32 - 0.56 GeV	1.02×10^{23}	$\simeq 4500$	05–11-04-2017 / 57848–57854	$(3.42 \pm 0.22) \times 10^{-10}$	349.0 ± 22.4	B.4.1.
Fermi-LAT	0.56 - 1.00 GeV	1.81×10^{23}	$\simeq 2800$	05–11-04-2017 /57848–57854	$(1.80 \pm 0.14) \times 10^{-10}$	327.1 ± 25.3	B.4.1.
Fermi-LAT	1.00 - 1.78 GeV	3.22×10^{23}	$\simeq 2000$	05–11-04-2017 / 57848–57854	$(9.56 \pm 0.83) \times 10^{-11}$	308.4 ± 26.8	B.4.1.
Fermi-LAT	1.78 - 3.16 GeV	5.73×10^{23}	$\simeq 1100$	05–11-04-2017 / 57848–57854	$(3.87 \pm 0.51) \times 10^{-11}$	221.7 ± 29.3	B.4.1.
Fermi-LAT	3.16 - 10 GeV	1.36×10^{24}	$\simeq 700$	05–11-04-2017 / 57848–57854	$(1.15 \pm 0.19) \times 10^{-11}$	156.5 ± 25.7	B.4.1.
Fermi-LAT	10 - 100 GeV	7.65×10^{24}	$\simeq 500$	05–11-04-2017 / 57848–57854	$(6.50 \pm 2.95) \times 10^{-11}$	49.7 ± 22.6	B.4.1.
Fermi-LAT	100 - 1000 GeV	7.65×10^{25}	$\simeq 350$	05–11-04-2017 / 57848–57854	$< 1.82 \times 10^{-13}$	< 139.5	B.4.1.
H.E.S.S.	0.105 - 0.153 TeV	3.07×10^{25}	$\simeq 360$	24–25-03-2017 / 57836-57837	$< 2.17 \times 10^{-14}$	< 6.67	B.4.2.
H.E.S.S.	0.153 - 0.27 TeV	4.90×10^{25}	$\simeq 360$	24–25-03-2017 / 57836-57837	$< 3.54 \times 10^{-15}$	< 1.74	B.4.2.
H.E.S.S.	0.27 - 0.57 TeV	9.45×10^{25}	$\simeq 360$	24–25-03-2017 / 57836-57837	$< 8.32 \times 10^{-16}$	< 0.79	B.4.2.
H.E.S.S.	0.57 - 1.0 TeV	1.83×10^{26}	$\simeq 360$	24–25-03-2017 / 57836-57837	$< 7.93 \times 10^{-17}$	< 0.14	B.4.2.
MAGIC	85 GeV	2.06×10^{25}	$\simeq 330$	01–02-04-2017 / 57849–57850	$< 5.28 \times 10^{-13}$	< 108.7	B.4.3.
MAGIC	115 GeV	2.79×10^{25}	$\simeq 330$	01–02-04-2017 / 57849–57850	$< 3.08 \times 10^{-14}$	< 8.58	B.4.3.
MAGIC	157 GeV	3.79×10^{25}	$\simeq 330$	01–02-04-2017 / 57849–57850	$< 2.23 \times 10^{-14}$	< 8.47	B.4.3.
MAGIC	213 GeV	5.14×10^{25}	$\simeq 330$	01–02-04-2017 / 57849–57850	$< 1.65 \times 10^{-14}$	< 8.47	B.4.3.
MAGIC	288 GeV	6.96×10^{25}	$\simeq 330$	01–02-04-2017 / 57849–57850	$< 8.41 \times 10^{-15}$	< 5.85	B.4.3.

Notes. [(1)] Spatial scale of the source emission (FWHM of the instrumental beam or PSF). For non-EHT radio observations, if the core is not resolved we use the flux peak obtained from the beam size as an upper limit on the core emission. For elliptical beams, we list the average of the axes as a representative angular scale. At higher energies the source is not spatially resolved; therefore, we quote the angular scale corresponding to the instrument's angular resolution (PSF) in the relative energy band.
[(2)] The source presents a photon flux of $\Phi = (5.01 \pm 0.57) \times 10^{-3}$ cm^2 s^{-1} and a photon index of $\Gamma = 1.46 \pm 0.19$, see Sect. B.3.